

1 **The Effects of Uncorrelated Measurement Noise on SWOT Estimates of**
2 **Sea-Surface Height, Velocity and Vorticity**

3 Dudley B. Chelton^a Roger M. Samelson,^a and J. Thomas Farrar,^b

4 ^a *College of Earth, Ocean and Atmospheric Sciences, Oregon State University, Corvallis, Oregon*

5 ^b *Woods Hole Oceanographic Institution, Woods Hole, Massachusetts*

6 *Corresponding author: Dudley B. Chelton, dudley.chelton@oregonstate.edu*

7 ABSTRACT: The Ka-band Radar Interferometer on the Surface Water and Ocean Topography (SWOT) satellite will revolutionize satellite altimetry by measuring sea surface height
8 (SSH) with unprecedented accuracy and resolution across two 50-km swaths separated by a 20-km
9 gap. The original plan to provide an SSH product with a footprint diameter of 1 km has changed
10 to providing two SSH data products with footprint diameters of 0.5 km and 2 km. The swath-
11 averaged standard deviations and wavenumber spectra of the uncorrelated measurement errors for
12 these footprints are derived from the SWOT science requirements that are expressed in terms of
13 the wavenumber spectrum of SSH after smoothing with a filter cutoff wavelength of 15 km. The
14 availability of 2-dimensional fields of SSH within the measurement swaths will provide the first
15 spaceborne estimates of instantaneous surface velocity and vorticity through the geostrophic equa-
16 tions. The swath-averaged standard deviations of the noise in estimates of velocity and vorticity
17 derived by propagation of the uncorrelated SSH measurement noise through the finite difference
18 approximations of the derivatives are shown to be too large for the SWOT data products to be
19 used directly in most applications, even with the footprint diameter of 2 km. It is shown from
20 wavenumber spectra and maps constructed from simulated SWOT data that additional smoothing
21 will be required for most applications of SWOT estimates of velocity and vorticity. Equations are
22 presented for the swath-averaged standard deviations and wavenumber spectra of residual noise in
23 SSH and geostrophically computed velocity and vorticity after isotropic 2-dimensional smoothing
24 for any user-defined filter cutoff wavelength of the smoothing.
25

26 **1. Introduction**

27 Presently available sea surface height (SSH) fields constructed from measurements by multiple
28 nadir-viewing satellite altimeters are able to resolve midlatitude variability on wavelength scales
29 down to about 200 km and monthly time scales (Chelton et al. 2011; Ballarotta et al. 2019).
30 This resolution capability will soon be greatly improved by SSH measurements from the Surface
31 Water and Ocean Topography (SWOT) satellite (Fu and Ferrari 2008; Durand et al. 2010; Fu
32 and Ubelmann 2014) that has a target launch date in November 2022. The primary instrument on
33 SWOT is the Ka-band Radar Interferometer (KaRIn) that will determine SSH from measurements
34 at a microwave frequency of 35.75 GHz using radar interferometry and synthetic aperture radar
35 technology (see appendix B; see also Fu and Rodríguez 2004). KaRIn will estimate SSH with a
36 footprint diameter of order 1 km across a pair of swaths 50 km wide separated by a 20-km gap
37 centered on the satellite ground track. The high accuracy and spatial resolution of the KaRIn data
38 and its wide measurement swath will significantly improve the space-time resolution capability
39 of SSH fields. This will greatly benefit studies of mesoscale ocean dynamics. Among other
40 applications, the smaller errors in maps of SSH constructed from SWOT data will reduce the
41 mislocations of mesoscale eddies in presently available SSH fields (e.g., Pascual et al. 2006).
42 The innovative measurements from KaRIn will also provide insight into ocean dynamics in the
43 submesoscale regime, and the role of these small scales in influencing or connecting to the dynamics
44 at larger scales.

45 While the primary goal of the SWOT mission is to improve the present SSH mapping capabilities,
46 SWOT will also enable the first spaceborne estimates of instantaneous surface vector velocity and
47 relative vorticity (referred to hereinafter as vorticity) that can be computed geostrophically from
48 the gridded SSH fields within the two SWOT measurement swaths. Estimates of these variables
49 from the SSH fields constructed from merged multi-mission altimeter data are limited by the
50 above-noted 200-km wavelength and monthly time scale resolution of these SSH fields. Surface
51 vector velocity can be estimated geostrophically from a single nadir-viewing altimeter on the coarse
52 grid of crossovers of ascending and descending ground tracks. However, in addition to the effects
53 of SSH measurement noise on errors in the geostrophically computed across-track velocities, the
54 accuracies of the vector velocity estimates at the crossovers are limited by sampling errors from
55 non-simultaneity of the ascending and descending overpasses and errors from the geometrical

56 transformation of the two across-track velocity estimates that are in general non-orthogonal at
57 the crossovers. The sampling errors and geometrical transformation errors both vary latitudinally
58 because of latitudinal variations of the time separation and angle between ascending and descending
59 ground tracks (Schlax and Chelton 2003).

60 The ability to estimate vector velocity and vorticity instantaneously by altimetry is thus unique
61 to the gridded SSH estimates across the two parallel KaRIn measurement swaths. Although the
62 SWOT mission was not designed to determine the surface velocity and vorticity fields, many
63 researchers intend to investigate ocean dynamics from SWOT estimates of these variables. The
64 equations from which the standard deviations and wavenumber spectra of noise can be computed for
65 all of the variables of interest (SSH, geostrophically computed velocity components u_g and v_g , and
66 the vorticity ζ_g) are presented in this study for any choice of footprint diameter in the ground-based
67 processing and subsequent additional spatial smoothing, referred to here as post-processing.

68 Our reference to u_g and v_g as “geostrophically computed velocity components” rather than
69 “geostrophic velocity components” is deliberate. There are several reasons the pressure field might
70 not be in geostrophic balance with the velocity field. For example, the geostrophic approximation
71 is valid only for small Rossby number. Because of the high incidence of large Rossby numbers at
72 small scales (see Figs. 4 and 5 of Chelton et al. 2019), the velocity components computed from the
73 geostrophic equations (see appendix D) give velocity estimates that may not be truly geostrophic on
74 all scales. Another concern is the possibility of erroneous contributions to the computed velocity
75 from gradients of the ageostrophic SSH signatures of internal tides and internal waves with short
76 wavelengths that may be resolvable in the SWOT data. Because of the large degree of smoothing
77 that will have to be applied in post-processing to mitigate the effects of measurement noise on
78 estimates of velocity and vorticity computed geostrophically from SWOT data (see sections 3–5),
79 most of the ageostrophic signals will be attenuated by the filtering. We therefore neglect errors of
80 the geostrophic approximation in the analysis that follows.

81 It is noteworthy that the surface velocity field on the large scales that are resolvable in SWOT data
82 includes wind-driven Ekman currents. These large-scale ageostrophic contributions to velocity
83 cannot be addressed from velocities computed geostrophically from SWOT data (Yu et al. 2021).

84 The SWOT satellite will also include a dual-frequency nadir altimeter that will measure SSH at
85 Ku-band and C-band frequencies of 13.6 GHz and 5.3 GHz with a footprint size and measurement

86 precision that are very different from KaRIn. The footprint for 1-second averages of nadir altimeter
87 measurements from the SWOT orbit altitude of 890 km for a significant wave height (SWH) of
88 2 m has across-track and along-track dimensions of approximately 3.5 km \times 10 km (see Figs.
89 22 and 23 of Chelton et al. 2001). These footprint dimensions increase with increasing SWH.
90 The nadir altimeter measurements are expected to have a noise standard deviation of 1.7 cm (see
91 Table 5 of JPL Internal Document 2017a). In comparison, the noise standard deviation of KaRIn
92 measurements of SSH for a much smaller footprint diameter of 2 km is expected to be about 1.4
93 cm (see section 2 and appendix C). Because the precision and footprint size for KaRIn differ so
94 much from those of the nadir altimeter, the latter is not considered in this study. Hereinafter, we
95 will generally refer to SWOT estimates of SSH with the implicit understanding that we consider
96 only the estimates from KaRIn.

97 This study also considers only the effects of uncorrelated measurement errors (which we will
98 refer to interchangeably as measurement noise) in KaRIn estimates of SSH and how they affect
99 spatially smoothed estimates of instantaneous SSH as well as SWOT estimates of surface velocity
100 and vorticity computed from instantaneous SSH for a chosen footprint diameter, both without
101 additional smoothing and with spatial smoothing applied in post-processing. The effects of long-
102 wavelength measurement errors are not addressed in this study. Because of the high-pass filtering
103 operation of the derivative operator, long-wavelength measurement errors have relatively little
104 effect on SWOT estimates of velocity and vorticity. We also do not consider the sampling errors
105 that arise from space-time smoothing of SWOT data from multiple overpasses of SWOT, which
106 are addressed in section 8 of Chelton et al. (2019).

107 The analysis in this study draws heavily from the appendices of Chelton et al. (2019), referred
108 to hereinafter as C19. The standard deviation σ_h of the uncorrelated noise in SWOT estimates
109 of SSH depends on the chosen footprint diameter. Although σ_h for a specified footprint diameter
110 is the fundamental characterization of the uncorrelated measurement errors, this information is
111 difficult to find and ambiguous in the current versions of the SWOT documents. Furthermore,
112 the footprint diameter of the SWOT estimates of SSH in the data products that will be provided
113 by the SWOT Project Office has evolved from the original plan that was to provide only a single
114 product with a footprint diameter of 1 km. The new plan is to provide two data products, one
115 with a footprint diameter of 0.5 km and the other with a footprint diameter of 2 km. To date,

116 the only documentation of this change is the recent SWOT Product Description Document (JPL
117 Internal Document 2020). To the enlightened reader, hints of the change to footprint diameters
118 of 0.5 km and 2 km can be inferred from sections 2.7.1a and 2.7.1b of the current version of
119 the Science Requirements Document (JPL Internal Document 2018). But the current versions of
120 the Mission Performance and Error Budget Document (JPL Internal Document 2017a) and the
121 Onboard Processing and Algorithm Theoretical Basis Document (JPL Internal Document 2017b)
122 both describe only the original planned footprint diameter of 1 km.

123 An objective of this study is to present the equations for the standard deviations and along-track
124 wavenumber spectra of the noise of all of the variables of interest (SSH, geostrophically computed
125 velocity components, and vorticity) in terms of the standard deviation σ_h of SSH noise for each of
126 the three footprint diameters of 0.5 km, 1 km and 2 km. These equations are presented in a series
127 of appendices, beginning with a summary in appendix A of the science requirements for KaRIn.
128 The requirement for the uncorrelated errors in KaRIn measurements of SSH that are the focus
129 of this study are specified in a non-conventional manner in terms of the swath-averaged along-
130 track wavenumber spectrum of the noise after smoothing the data with a half-power filter cutoff
131 wavelength of 15 km. After an overview of the onboard and ground-based processing of SWOT
132 data in appendix B, the swath-averaged standard deviations of the measurement noise in the SSH
133 estimates without 15-km smoothing are derived in appendix C from the spectral characterization
134 for the three footprint diameters of 0.5 km, 1 km and 2 km. Our analysis assumes that the spectral
135 characteristics of uncorrelated measurement errors are “white” (i.e., constant) for all wavenumbers
136 up to the Nyquist wavenumber of $(2\Delta y)^{-1}$ that is associated with a sample grid spacing of Δy in
137 the along-track dimension that is equal to the footprint diameter. Note, however, that the science
138 requirements specify a white noise spectrum only for wavenumbers up to 1/15 cpkm (cycles per
139 km), i.e., wavelengths longer than 15 km (see appendix A).

140 The equations for the swath-averaged standard deviations of the noise in velocity components
141 computed from SSH by finite-difference approximations of the derivatives in the geostrophic
142 equations, and of the noise in vorticity estimated from finite-difference approximations of the
143 derivatives of the geostrophically computed velocity components, are presented in appendix D.
144 The discussion of the standard deviations of the noise in SWOT estimates of all three variables

145 (SSH, velocity and vorticity) are extended in appendix E in which equations are presented for the
146 along-track wavenumber spectral characteristics of the noise without 15-km smoothing.

147 As summarized in section 2, the conclusion from the analysis in appendices D and E is that
148 velocity and vorticity computed geostrophically from the SWOT SSH data products will be too
149 noisy to be used directly for most applications, even for the coarsest footprint diameter of 2 km
150 considered here. Most analyses of SWOT data over oceans will therefore be based on the 2-km SSH
151 product provided by the SWOT Project, with additional smoothing applied in post-processing to
152 reduce the noise and improve the signal-to-noise ratio. The additional smoothing will be especially
153 important for SWOT estimates of velocity and vorticity. The equations for the standard deviations
154 and wavenumber spectra of the noise in smoothed SWOT estimates of all three variables are
155 presented in sections 3 and 4.

156 Example maps of SSH and geostrophically computed velocity magnitude and vorticity con-
157 structed from simulated SWOT data are presented in section 5 for selected choices of smoothing
158 in post-processing. The simulated SWOT data include uncorrelated noise with the swath-averaged
159 standard deviation σ_h derived in appendix C for the footprint diameter of 2 km that will likely be the
160 SWOT data product preferred by most users. The purpose of presenting these maps is to provide
161 a visual sense of what to expect from SWOT data with various amounts of smoothing applied in
162 post-processing. The maps also provide insight into the contamination that can be expected from
163 edge effects of smoothing within the 50-km width of the two measurement swaths.

164 For easy application, the equations in appendices C–E and sections 3 and 4 are all expressed
165 in terms of the across-track and along-track grid spacings Δx and Δy and standard deviation σ_h
166 of the SWOT data product with the specified footprint diameter. The table and figures presented
167 in this study are based on the pre-launch estimates of σ_h that are derived in appendix C for
168 the footprint diameters of 0.5 km, 1 km and 2 km. The SSH noise standard deviation σ_h that
169 appears in the equations from which the table and figures were generated can be replaced with the
170 actual value determined after launch from in-orbit data for any specified footprint diameter, grid
171 spacing of the data, swath location and significant wave height. Moreover, the equations presented
172 here will be applicable to future versions of the SWOT data products in which the measurement
173 noise standard deviations σ_h are likely to decrease through improvements in the onboard and
174 ground-based processing of SWOT data.

175 **2. The effects of uncorrelated measurement noise on SWOT estimates of SSH, velocity and** 176 **vorticity**

177 The errors in SWOT estimates of SSH, velocity and vorticity have previously been investigated
178 by C19 for the case of a footprint diameter of 1 km that was the original plan for the gridded
179 SWOT data product. As noted in the introduction, the SWOT Project has recently replaced the
180 1-km data product with two gridded SSH products with footprint diameters of 0.5 km and 2 km.
181 The error analysis in C19 is extended here in appendices C–E to derive the standard deviations and
182 wavenumber spectra of the noise for these new footprint diameters. We refer to SWOT estimates
183 of SSH, velocity and vorticity with a chosen footprint diameter as “unsmoothed.” In actuality, they
184 are produced by isotropic 2-dimensional smoothing of the raw SWOT data that have a resolution
185 of tens of meters (see appendix B) using a filter that has a half-power filter cutoff wavelength
186 of approximately twice the footprint diameter (see appendix B.1 of C19). SWOT estimates of
187 SSH, velocity and vorticity generated from SWOT data with any of the three footprint diameters
188 considered in this study are referred to as “smoothed” when they are subsequently filtered in
189 post-processing to improve the signal-to-noise ratio by reducing the small-scale noise.

202 Expressions for the standard deviations of the noise in unsmoothed SWOT estimates of SSH, the
203 geostrophically computed velocity components u_g and v_g , and the vorticity ζ_g computed from u_g
204 and v_g are presented in appendices C and D for each of the three footprint diameters of 0.5 km, 1
205 km and 2 km. The results are summarized in the top half of Table 1. The noise standard deviation
206 for SWOT measurements of SSH with a footprint diameter of 2 km that is the data product likely
207 to be preferred by most users is 1.37 cm. As noted in the introduction, this is smaller than the noise
208 deviation of about 1.7 cm in SSH measurements from conventional nadir altimeters with their
209 much larger footprint dimensions. The noise standard deviations for SWOT estimates of velocity
210 components and vorticity are comparable to or larger than the signal standard deviations in most
211 regions of the world ocean for all three footprint diameters considered here. The challenges of
212 distinguishing signal and noise are further underscored in appendix E by the wavenumber spectra
213 of unsmoothed SWOT estimates of velocity and vorticity that are shown to be more energetic than
214 the signal spectra over most wavenumbers (see Fig. E1).

215 The conclusions from the analysis in appendices C–E and the noise statistics summarized in
216 the top half of Table 1 and Fig. E1 are thus that SWOT data will have to be smoothed in post-

190 TABLE 1. The swath-averaged standard deviations of the noise in SWOT estimates of SSH, geostrophically
 191 computed velocity components u_g and v_g and relative vorticity ζ_g . The top half of the table lists the noise
 192 standard deviations for “unsmoothed” data with footprint diameters of 0.5 km, 1.0 km and 2.0 km. Results for
 193 the case of 0.5 km footprint diameter are shown for a sample grid spacing of 0.5 km \times 0.5 km on which the
 194 measurement errors are uncorrelated, and on an oversampled grid spacing of 0.25 km \times 0.25 km. The bottom
 195 half of the table lists the residual noise standard deviations for the case of 2 km footprint diameter after additional
 196 smoothing in post-processing using a Parzen smoother with selected half-power filter cutoff wavelengths. The
 197 geostrophic calculations are based on a Coriolis parameter of $f_{37N} = 8.77 \times 10^{-5} \text{ s}^{-1}$ at the central latitude of
 198 37°N of the model of the California Current System used here (see Fig. 3). The noise in u_g and v_g for other
 199 latitudes can be determined by multiplying the values in the fourth column by f_{37N}/f , where f is the magnitude
 200 of the Coriolis parameter at the latitude of interest. The noise of ζ_g/f can be determined by multiplying the
 201 values in the last column by $(f_{37N}/f)^2$.

Unsmoothed Noise

Footprint Diameter	Grid Spacing	σ_h	$\sigma_{u_g}, \sigma_{v_g}$ at 37°N	σ_{ζ_g} at 37°N	σ_{ζ_g}/f at 37°N
0.5 km	0.25 km	5.48 cm	16.99 m s ⁻¹	1.05×10 ⁻¹ s ⁻¹	1198.1
0.5 km	0.5 km	5.48 cm	8.67 m s ⁻¹	2.74×10 ⁻² s ⁻¹	312.3
1.0 km	1.0 km	2.74 cm	2.17 m s ⁻¹	3.43×10 ⁻³ s ⁻¹	39.0
2.0 km	2.0 km	1.37 cm	0.54 m s ⁻¹	4.28×10 ⁻⁴ s ⁻¹	4.9

Smoothed Noise

Filter Cutoff	Grid Spacing	σ_h	$\sigma_{u_g}, \sigma_{v_g}$ at 37°N	σ_{ζ_g} at 37°N	σ_{ζ_g}/f at 37°N
15 km	2.0 km	0.37 cm	0.118 m s ⁻¹	8.06×10 ⁻⁵ s ⁻¹	0.920
30 km	2.0 km	0.19 cm	0.034 m s ⁻¹	1.51×10 ⁻⁵ s ⁻¹	0.172
50 km	2.0 km	0.11 cm	0.013 m s ⁻¹	3.59×10 ⁻⁶ s ⁻¹	0.041
70 km	2.0 km	0.08 cm	0.007 m s ⁻¹	1.34×10 ⁻⁶ s ⁻¹	0.015

217 processing for most ocean applications in order to reduce the noise, especially for SWOT estimates
218 of velocity and vorticity. Such smoothing attenuates the signal as well as the noise. The noise
219 power is attenuated more than the signal power because the SSH, velocity and vorticity signals
220 are more dominated by spatially correlated low-wavenumber variability (see the thick black lines
221 in Fig. E1). The signal-to-noise ratios therefore improve with increased smoothing. Estimation
222 of ζ_g is the most challenging because the signal is less dominated by large-scale variability (see
223 Fig. E1d) and is therefore more attenuated by the smoothing. The effects of smoothing on the
224 standard deviation and wavenumber spectra of residual noise in SWOT estimates of SSH, velocity
225 and vorticity are quantified in sections 3 and 4.

226 **3. The standard deviations of smoothed noise in SWOT estimates of SSH, velocity and vor-** 227 **ticity**

228 The equations for the swath-averaged standard deviations of residual noise in SWOT estimates
229 of SSH, u_g , v_g and ζ_g after the 2-dimensional smoothing that will be required for most ocean
230 applications of SWOT data are derived in appendix G.3 of C19. The analysis is based on isotropic
231 2-dimensional smoothing using the Parzen smoother that is discussed in detail in appendix A of
232 C19. The results would be very similar for other choices of smoother, as long as the parame-
233 ters of the smoother are calibrated to give the same half-power filter cutoff wavelength λ_c . A
234 useful characteristic of the Parzen smoother is that its filter transfer function is almost identical
235 to that of a Gaussian smoother (see Fig. C2 in appendix C of C19). A convenient property of
236 the Gaussian smoother is that isotropic 2-dimensional smoothing that depends only on the radial
237 distance of each data point from the estimation location can be achieved equivalently through
238 successive 1-dimensional smoothing operations in each of two orthogonal dimensions. The sim-
239 ilarity of the filter transfer functions of the Parzen and Gaussian smoothers implies that isotropic
240 2-dimensional smoothing with the Parzen smoother can essentially be achieved equivalently with
241 separate 1-dimensional smoothing in two orthogonal dimensions. A distinct advantage of separate
242 1-dimensional smoothing is that it facilitates the derivations of the analytical equations in section
243 4 below for the wavenumber spectra of residual noise in smoothed estimates of SSH, u_g , v_g and
244 ζ_g . While the Parzen smoother nearly replicates the exact equivalence of isotropic 2-dimensional

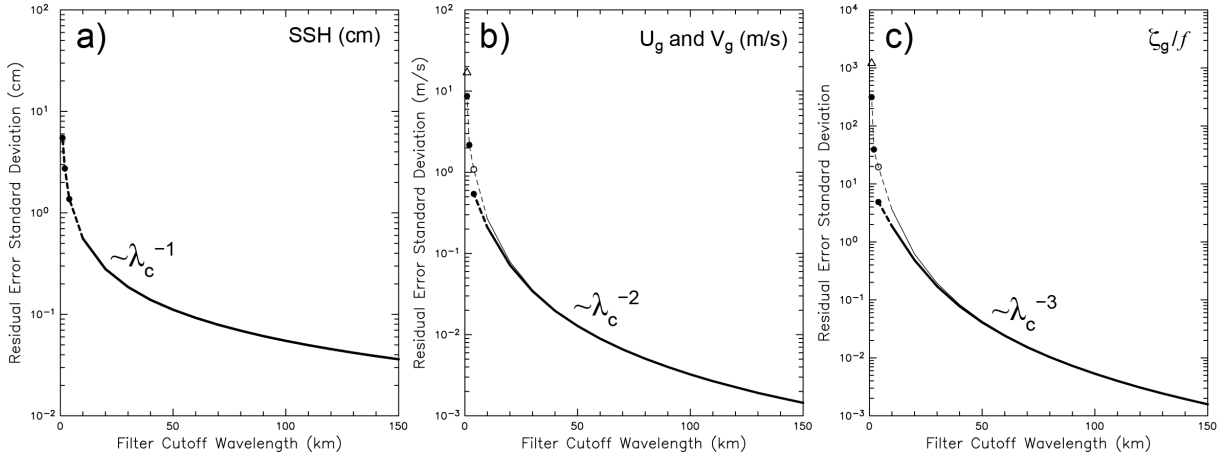
245 smoothing and sequential 1-dimensional smoothing in two orthogonal dimensions for the Gaussian
246 smoother, this equivalence is only approximate for most other smoothing algorithms.

247 To provide context for the analysis in this section, it is useful to display the noise standard
248 deviations graphically for unsmoothed SWOT estimates of SSH, velocity and vorticity as functions
249 of the half-power filter cutoff wavelengths associated with each of the footprint diameters of 0.5 km,
250 1 km and 2 km. It is shown in appendix B.1 of C19 that SSH estimates with a footprint diameter
251 of 1 km can be achieved with isotropic 2-dimensional smoothing of raw SWOT data using a
252 Parzen smoother with a half-power filter cutoff wavelength of 2 km, i.e., twice the desired footprint
253 diameter. It is also shown in appendix B.1 of C19 that the noise in these estimates of SSH is
254 uncorrelated on a grid spacing of $1 \text{ km} \times 1 \text{ km}$. SWOT estimates of SSH, velocity and vorticity
255 with the footprint diameters of 0.5 km and 2 km can correspondingly be obtained by 2-dimensional
256 smoothing of raw SWOT data using Parzen smoothers with half-power filter cutoff wavelengths
257 of 1 km and 4 km, respectively, and the noise for these footprints is uncorrelated on grids with
258 spacings equal to the respective footprint diameters. (As discussed in appendices B and C of this
259 study, the SWOT Project may decide to smooth the SSH with a half-power filter cutoff wavelength
260 somewhat longer than 4 km for the $2 \text{ km} \times 2 \text{ km}$ data product; such increased smoothing would
261 not significantly alter any of the conclusions of this study.)

262 The standard deviations listed in the top half of Table 1 for the SSH noise with the three footprint
263 diameters of 0.5 km, 1 km and 2 km and sample grid spacings equal to the footprint diameters
264 (rows 2–4 in Table 1) are displayed at their associated filter cutoff wavelengths of 1 km, 2 km
265 and 4 km by the solid circles in Fig. 1a. The corresponding noise standard deviations for the
266 geostrophically computed velocity components u_g and v_g and the vorticity ζ_g are shown by the
267 solid circles in Figs. 1b and c. The noise standard deviation for SSH with the footprint diameter
268 of 0.5 km is the same on the oversampled $0.25 \text{ km} \times 0.25 \text{ km}$ grid as on the $0.5 \text{ km} \times 0.5 \text{ km}$ grid.
269 However, the noise standard deviations for u_g , v_g and ζ_g with the footprint diameter of 0.5 km are
270 larger on the oversampled $0.25 \text{ km} \times 0.25 \text{ km}$ grid (see row 1 in Table 1 and the triangles in Figs.
271 1b and 1c). This is because the finite-difference approximations of the derivatives are computed
272 on a smaller grid spacing, which increases the noise in accord with (D3), (D4) and (D7).

285 Because of the excessively large noise standard deviations for all three variables with the footprint
286 diameter of 0.5 km, this case is not considered further in the discussion that follows. The standard

Standard Deviations of Smoothed SSH, Velocity and Vorticity Noise



273 FIG. 1. The standard deviations of residual noise as functions of half-power filter cutoff wavelength λ_c for
 274 isotropic 2-dimensional smoothing of SWOT data with a Parzen smoother: a) SSH; b) velocity component
 275 estimates computed geostrophically from SSH based on the Coriolis parameter f_{37N} for a latitude of 37°N; and
 276 c) vorticity computed from the geostrophic estimates of velocity and normalized by f_{37N} . The three solid circles
 277 that are connected by dashed lines correspond to the error standard deviations for footprint diameters of 0.5 km,
 278 1 km and 2 km (filter cutoff wavelengths of 1 km, 2 km and 4 km). The solid lines are the standard deviations
 279 of residual noise after smoothing for footprint diameters of 1 km on a 1 km × 1 km grid (thin lines) and 2 km
 280 on a 2 km × 2 km grid (thick lines). The open triangles in b) and c) are the noise standard deviations for a
 281 footprint diameter of 0.5 km on an oversampled 0.25 km × 0.25 km grid. The open circles in b) and c) are the
 282 standard deviations for a footprint diameter of 1 km on a 1 km × 1 km grid smoothed with the half-power filter
 283 cutoff wavelength of 4 km; these noise standard deviations are larger than for the footprint diameter of 2 km on
 284 a 2 km × 2 km grid because the finite differences are computed on a smaller grid spacing.

287 deviations of the residual noise in SWOT estimates of SSH, u_g , v_g and ζ_g after isotropic 2-
 288 dimensional smoothing in post-processing are determined in this section only for the footprint
 289 diameters of 1 km and 2 km.

290 The variance of the residual noise in SSH after isotropic 2-dimensional smoothing, which will
 291 be denoted here with an overbar, can be expressed in terms of the variance σ_h^2 of unsmoothed SSH
 292 by Eq. (D.5a) in appendix D of C19, which is

$$\overline{\sigma}_h^2 = \alpha \sigma_h^2. \quad (1a)$$

293 For grid spacings Δx and Δy in the x and y dimensions and smoothing using a Parzen smoother
 294 with a half-power filter cutoff wavelength of λ_c in each of two orthogonal dimensions (which is
 295 essentially the same as isotropic 2-dimensional smoothing with a Gaussian smoother, as discussed
 296 at the beginning of this section), the scaling factor α in (1a) is given by Eq. (D.14c) of C19, which
 297 is

$$\alpha \approx \frac{4\Delta x\Delta y}{\lambda_c^2}. \quad (1b)$$

298 Note that this expression is applicable only for a grid spacing $\Delta x \times \Delta y$ on which the measurement
 299 errors are uncorrelated. For the case of Δx and Δy equal to the footprint diameter, i.e., the minimum
 300 grid spacing on which the SSH measurement noise is uncorrelated, it is evident from (1a) and (1b)
 301 that $\bar{\sigma}_h^2$ for any specified λ_c is the same for any footprint diameter. This can be seen mathematically
 302 by noting that doubling the footprint diameter from 1 km to 2 km, for example, reduces the noise
 303 variance σ_h^2 on the right side of (1a) by a factor of 4 but doubles the sample spacings $\Delta x = \Delta y$ for
 304 uncorrelated noise in the numerator of (1b), thus increasing the product $\Delta x\Delta y$ by a factor of 4. The
 305 two factors of 4 cancel for any choice of filter cutoff wavelength λ_c . The variance of smoothed
 306 SSH is therefore independent of footprint diameter if the grid spacings Δx and Δy are chosen to
 307 be equal to the footprint diameter. The variance (1) of smoothed SSH noise is thus proportional to
 308 λ_c^{-2} so that the SSH noise standard deviation $\bar{\sigma}_h$ decreases as λ_c^{-1} . The resulting dependence of $\bar{\sigma}_h$
 309 on λ_c is shown in Fig. 1a. The analytical expression for this curve obtained from (1a) and (1b) is

$$\bar{\sigma}_h = a_h \lambda_c^{-1}, \quad (2)$$

310 where $a_h = 5.48$ cm km. Note the relationship between a_h and the SSH measurement noise standard
 311 deviation of $\sigma_h = 5.48$ cm for a half-power filter cutoff wavelength of $\lambda_c = 1$ km, i.e., a footprint
 312 diameter of 0.5 km (see Table 1).

313 The variance of the residual noise in the geostrophically computed velocity component v_g after
 314 isotropic 2-dimensional smoothing can be expressed in terms of the variance $\bar{\sigma}_h^2$ of the smoothed
 315 SSH measurement noise by Eq. (G.17a) of C19, which is

$$\bar{\sigma}_{v_g}^2 = \frac{g^2}{f^2} \frac{1}{2\Delta x^2} \left[1 - \bar{\rho}_h(2\Delta x) \right] \bar{\sigma}_h^2, \quad (3a)$$

316 where $\bar{\rho}_h(2\Delta x)$ is the autocorrelation of the smoothed estimates of SSH noise at a lag of $2\Delta x$.
 317 Substituting (1) for $\bar{\sigma}_h^2$ expresses $\bar{\sigma}_{v_g}^2$ in terms of the variance σ_h^2 of unsmoothed SSH,

$$\bar{\sigma}_{v_g}^2 = \frac{g^2}{f^2} \frac{2\Delta y}{\lambda_c^2 \Delta x} \left[1 - \bar{\rho}_h(2\Delta x) \right] \sigma_h^2. \quad (3b)$$

318 The analogous expressions for the variance of the residual noise in the geostrophically computed
 319 velocity component u_g after isotropic 2-dimensional smoothing are

$$\bar{\sigma}_{u_g}^2 = \frac{g^2}{f^2} \frac{1}{2\Delta y^2} \left[1 - \bar{\rho}_h(2\Delta y) \right] \bar{\sigma}_h^2 \quad (4a)$$

$$= \frac{g^2}{f^2} \frac{2\Delta x}{\lambda_c^2 \Delta y} \left[1 - \bar{\rho}_h(2\Delta y) \right] \sigma_h^2, \quad (4b)$$

320 where $\bar{\rho}_h(2\Delta y)$ is the autocorrelation of the smoothed estimates of SSH noise at a lag of $2\Delta y$.
 321 For homogeneous noise and a uniform sample grid spacing $\Delta y = \Delta x$, the variances (3) and (4) of
 322 smoothed noise in v_g and u_g are the same.

323 The right sides of the forms (3a) and (4a) for the variances of smoothed estimates of v_g and u_g
 324 are the same as the right sides of the expressions (D3b) and (D4) for the variances of noise in
 325 unsmoothed v_g and u_g , except with overbars to indicate the variances and lagged autocorrelations
 326 of smoothed estimates. The lagged autocorrelations for smoothed SSH inside the square brackets
 327 in (3) and (4) are always larger than their counterpart lagged autocorrelations for unsmoothed SSH
 328 inside the square brackets in (D3b) and (D4). The forms (3b) and (4b) for $\bar{\sigma}_{v_g}^2$ and $\bar{\sigma}_{u_g}^2$ allow
 329 calculation of the variances of the residual noise in smoothed geostrophically computed SWOT
 330 estimates of the velocity components for any choice of half-power filter cutoff wavelength λ_c from
 331 the variance σ_h^2 of the unsmoothed SSH noise for the footprint diameter of interest, the specified
 332 grid spacings Δx and Δy , and the lagged autocorrelations $\bar{\rho}_h(2\Delta x)$ and $\bar{\rho}_h(2\Delta y)$ of the smoothed
 333 SSH for the particular choice of λ_c .

334 Some general comments can be made on the interpretations of (3) and (4). As discussed above
 335 from (1), the residual variance $\bar{\sigma}_h^2$ of the smoothed SSH noise is independent of footprint diameter
 336 for any specified filter cutoff wavelength λ_c when the grid spacings are chosen commensurately to
 337 be equal to the footprint diameter. In contrast, the variances of residual noise in u_g and v_g depend
 338 on the footprint diameter through their dependencies on the variance σ_h^2 of unsmoothed SSH noise

339 that itself depends on the footprint diameter. The factor-of-4 difference between the values of σ_h^2
340 for footprint diameters of 1 km and 2 km on the right sides of (3b) and (4b) exists for any choice
341 of filter cutoff wavelength λ_c . With increased smoothing, however, this factor-of-4 difference is
342 moderated by the lagged autocorrelations inside the square brackets that increase with increasing
343 λ_c . Because the lag distances $2\Delta x$ and $2\Delta y$ are twice as large for the commensurate grid spacings
344 associated with the 2-km footprint diameter as for the 1-km footprint diameter, the autocorrelation
345 values at these lags are always smaller for the larger footprint diameter. For small half-power filter
346 cutoff wavelength λ_c , these differences in the lagged autocorrelation values are substantial.

347 Although not readily apparent, the terms in square brackets in (3) and (4) converge with increasing
348 λ_c toward values that are a factor of 4 larger for the 2-km footprint diameter than for the 1-km
349 footprint diameter. This factor-of-4 increase offsets the factor-of-4 smaller value of σ_h^2 for the 2-km
350 footprint diameter. The net effect is that the variances of the residual noise in smoothed estimates
351 of u_g and v_g from the two footprint diameters converge with increasing λ_c . An intuitive explanation
352 for the convergence of the variances of the residual noise in u_g and v_g for the two footprint diameters
353 with increasing λ_c is given later in section 4 from the equations for the wavenumber spectra of
354 smoothed u_g and v_g noise.

355 The dependencies of the standard deviations $\bar{\sigma}_{u_g}$ and $\bar{\sigma}_{v_g}$ of the residual noise in smoothed
356 estimates of u_g and v_g on filter cutoff wavelength λ_c obtained from (3) and (4) are shown as
357 functions of λ_c in Fig. 1b for SWOT data with footprint diameters of 1 km and 2 km (the thin and
358 thick lines, respectively). As in appendix D, we used the value of $f_{37N} = 8.75 \times 10^{-5} \text{ s}^{-1}$ for the
359 Coriolis parameter at 37°N in (3) and (4). This corresponds to the central latitude of the domain of
360 the model of the California Current System used in this study (see Fig. 3). The values of $\bar{\sigma}_{u_g}$ and
361 $\bar{\sigma}_{v_g}$ for a given footprint diameter are indistinguishable from each other. The above-noted rapid
362 convergence of the standard deviations of the residual noise in smoothed estimates of u_g and v_g
363 with increasing λ_c for the two footprint diameters is evident from Fig. 1b. The two curves become
364 barely distinguishable for $\lambda_c \gtrsim 20$ km. The dependence on λ_c at filter cutoff wavelengths longer
365 than 20 km can be very closely approximated by a power-law dependence on λ_c ,

$$\bar{\sigma}_{u_g} = \bar{\sigma}_{v_g} \approx \hat{a}_{u,v} \lambda_c^{-2}, \quad (5)$$

366 where $\hat{a}_{u,v} = 31.64 \text{ m s}^{-1} \text{ km}^2$ is the empirically determined (signified by the hat) least-squares
 367 estimate of the scaling parameter. For latitudes other than 37°N , this value of $\hat{a}_{u,v}$ must be multiplied
 368 by f_{37N}/f , where f is the Coriolis parameter at the latitude of interest.

369 For the analysis presented here, vorticity was estimated from 3-point centered differences of
 370 geostrophically computed velocity components at adjacent grid points, which were themselves
 371 estimated from 3-point centered differences of SSH at adjacent grid points (see the discussion in
 372 the footnote in appendix D). For a uniform grid spacing $\Delta y = \Delta x$ equal to the footprint diameter, the
 373 variance of the residual noise in geostrophically computed vorticity after isotropic 2-dimensional
 374 smoothing can be expressed in terms of the variance $\overline{\sigma}_h^2$ of the smoothed SSH measurement noise
 375 by Eq. (G.21) of C19, which is

$$\overline{\sigma}_{\zeta_g}^2 = \frac{g^2}{f^2} \frac{1}{(4\Delta x^2)^2} \left[20 + 4\overline{\rho}_h(4\Delta x) - 32\overline{\rho}_h(2\Delta x) + 8\overline{\rho}_h(2\sqrt{2}\Delta x) \right] \overline{\sigma}_h^2. \quad (6a)$$

376 This is the same as the expression (D7) for the variance of noise in unsmoothed ζ_g , except with
 377 overbars to indicate the variances and lagged correlations of smoothed estimates. The lagged
 378 autocorrelations for smoothed SSH inside the square brackets of (6a) are always larger than their
 379 counterpart lagged autocorrelations for unsmoothed SSH inside the square brackets in (D7). For
 380 this case of $\Delta y = \Delta x$, substitution of (1) for $\overline{\sigma}_h^2$ expresses $\overline{\sigma}_{\zeta_g}^2$ in terms of the variance σ_h^2 of
 381 unsmoothed SSH noise,

$$\overline{\sigma}_{\zeta_g}^2 = \frac{g^2}{f^2} \frac{1}{4\lambda_c^2 \Delta x^2} \left[20 + 4\overline{\rho}_h(4\Delta x) - 32\overline{\rho}_h(2\Delta x) + 8\overline{\rho}_h(2\sqrt{2}\Delta x) \right] \sigma_h^2. \quad (6b)$$

382 As in the cases of the variances (3) and (4) of the residual noise in smoothed estimates of u_g and
 383 v_g , the variance $\overline{\sigma}_{\zeta_g}^2$ of the residual noise in smoothed ζ_g in the form (6b) can be calculated for
 384 any choice of half-power filter cutoff wavelength λ_c from the variance σ_h^2 of the unsmoothed SSH
 385 noise for the footprint diameter of interest, the specified grid spacings Δx and Δy [assumed to be
 386 the same in (6)] and the three lagged autocorrelations of smoothed SSH on the right side of (6).
 387 Whereas $\overline{\sigma}_{u_g}^2$ and $\overline{\sigma}_{v_g}^2$ depend on the autocorrelation of smoothed SSH at the single lag $2\Delta x$, the
 388 variance $\overline{\sigma}_{\zeta_g}^2$ of the residual noise in smoothed estimates of ζ_g depends on the autocorrelations of
 389 smoothed SSH at lags of $2\Delta x$, $2\sqrt{2}\Delta x$ and $4\Delta x$.

390 The standard deviation of the residual noise in smoothed estimates of ζ_g obtained from (6) and
 391 normalized by the Coriolis parameter f are shown as a function of filter cutoff wavelength λ_c in
 392 Fig. 1c. We again used the value of f_{37N} for the Coriolis parameter. The differences between the
 393 standard deviations of the smoothed ζ_g noise for the footprint diameters of 1 km and 2 km (the
 394 thin and thick lines, respectively) are substantial for small λ_c but converge rapidly with increasing
 395 λ_c , becoming barely distinguishable for $\lambda_c \gtrsim 30$ km. The standard deviation of the vorticity noise
 396 normalized by the Coriolis parameter f at wavelengths longer than 30 km can be very closely
 397 approximated by a power-law dependence on λ_c ,

$$\frac{\overline{\sigma}_\zeta}{f} \approx \hat{a}_\zeta \lambda_c^{-3}, \quad (7)$$

398 where $\hat{a}_\zeta = 5222 \text{ km}^3$ is the empirically determined least-squares estimate of the scaling parameter.
 399 For latitudes other than 37°N , this value of \hat{a}_ζ must be multiplied by $(f_{37N}/f)^2$.

400 Numerical values of the standard deviations $\overline{\sigma}_h$, $\overline{\sigma}_{u_g}$, $\overline{\sigma}_{v_g}$, $\overline{\sigma}_{\zeta_g}$ and $\overline{\sigma}_{\zeta_g}/f$ of the residual noise
 401 in the smoothed variables are listed in the bottom half of Table 1 for four choices of the half-power
 402 filter cutoff wavelength λ_c . The case of $\lambda_c = 15$ km corresponds to the filtering in the specification
 403 of the science requirements for SWOT estimates of SSH that are discussed in appendix A. The
 404 cases of $\lambda_c = 30$ km, 50 km and 70 km that are listed in the table include all of the choices of
 405 smoothing that are applied for the spectra in section 4 and for the maps in section 5.

406 The variances $\overline{\sigma}_h^2$, $\overline{\sigma}_{u_g}^2$, $\overline{\sigma}_{v_g}^2$ and $\overline{\sigma}_{\zeta_g}^2$ of the residual noise of the smoothed variables computed
 407 from (1), (3), (4) and (6) could have been computed alternatively from Parseval's Theorem (C2)
 408 in appendix C by integrating the wavenumber spectra of the residual noise after smoothing that
 409 are presented below in section 4. An advantage of that approach is that the expressions for the
 410 spectra isolate the separate filtering from the smoothing and the 3-point centered differencing
 411 on the residual variances of the smoothed noise computed from SWOT data. For grid spacings
 412 Δx and Δy equal to the footprint diameter that is the minimum interval at which the SSH noise
 413 is uncorrelated, the products $\Delta x \Delta y \sigma_h^2$ that appear in the equations for the spectra of all of the
 414 smoothed variables (see section 4) are independent of footprint diameter, as discussed previously
 415 from (1). The only differences between the expressions for the footprint diameters of 1 km and 2
 416 km are thus the factors that involve the response function (E2) of the 3-point centered difference
 417 estimates of the derivatives. The differences between the thin and thick lines in Figs. 1b and c are

418 thus solely attributable to the filtering effects of finite-difference approximations of the derivatives
 419 on the different grids. This point is discussed further in section 4.

420 **4. The wavenumber spectra of smoothed noise in SWOT estimates of SSH, velocity and** 421 **vorticity**

422 The equations for the swath-averaged along-track wavenumber spectra of noise in SWOT esti-
 423 mates of SSH, u_g , v_g and ζ_g after isotropic 2-dimensional smoothing are derived in appendix
 424 I.2 of C19. As in section 3, we consider only the cases of footprint diameters of 1 km and 2 km
 425 since the noise is so large for a footprint diameter of 0.5 km. The spectrum of smoothed SSH noise
 426 is derived straightforwardly to obtain Eq. (I.27) of C19, which is

$$\bar{S}_h(l) = 4\Delta x \Delta y \sigma_h^2 W_{\lambda_c}^2(l) \int_0^{k_N} W_{\lambda_c}^2(k) dk \quad (8a)$$

$$= 2\Delta x S_h(l) W_{\lambda_c}^2(l) \int_0^{k_N} W_{\lambda_c}^2(k) dk, \quad (8b)$$

427 where $W_{\lambda_c}(k)$ and $W_{\lambda_c}(l)$ are the filter transfer functions of the smoother applied in the orthogonal
 428 x and y dimensions with a half-power filter cutoff wavelength of λ_c in each dimension. The form
 429 (8b) follows from Parseval's Theorem (C3) that relates the integral of the constant white noise
 430 spectrum $S_h(l)$ to the variance of the uncorrelated SSH errors.

431 The expressions (8a) and (8b) are based on separate 1-dimensional smoothing in the orthogonal x
 432 and y dimensions, which we define to be across-track and along-track, respectively. For the Parzen
 433 smoother used in this study, this is essentially equivalent to isotropic 2-dimensional smoothing with
 434 a Gaussian smoother, as discussed previously at the beginning of section 3. This is approximately
 435 true for most other choices of smoothing. The advantage of separate smoothing in two orthogonal
 436 dimensions is that it allows the simple analytical forms (8a) and (8b) for the spectrum of smoothed
 437 SSH noise and analogously simple analytical expressions for the spectra of smoothed u_g , v_g and
 438 ζ_g that are presented below. It can be seen from (8b) that smoothing in the across-track dimension
 439 attenuates the along-track spectrum $S_h(l)$ of unsmoothed noise for the specified footprint diameter
 440 by the constant multiplicative factor

$$c_{\lambda_c} = 2\Delta x \int_0^{k_N} W_{\lambda_c}^2(k) dk \quad (9)$$

441 at all wavenumbers l . Note that $2\Delta x = k_N^{-1}$, which is the Nyquist wavenumber associated with
 442 the sample interval Δx . In addition to this uniform attenuation at all wavenumbers, it can be seen
 443 from (8b) that $S_h(l)$ is attenuated at high wavenumbers l by the along-track filter transfer function
 444 $W_{\lambda_c}^2(l)$. The details of this wavenumber-dependent attenuation depend on the filter transfer function
 445 $W_{\lambda_c}(l)$ of the particular smoother applied to the unsmoothed SWOT estimates of SSH.

446 For the Parzen smoother used in C19 and in this study, it is shown in appendix A of C19 that the
 447 filter transfer function in the across-track dimension x is

$$W_{\lambda_c}(k) = \left(\frac{\sin(\pi k \lambda_c / 4)}{\pi k \lambda_c / 4} \right)^4. \quad (10)$$

448 The filter transfer function $W_{\lambda_c}(l)$ in the along-track dimension y is the same, except with across-
 449 track wavenumber k replaced with along-track wavenumber l . From Eq. (I.28) of C19, the
 450 integral of the square of the filter transfer function $W_{\lambda_c}(k)$ that appears in (8) and (9) has a simple
 451 approximate form in the case of the Parzen smoother,

$$\int_0^{k_N} W_{\lambda_c}^2(k) dk \approx \frac{1}{\lambda_c}. \quad (11)$$

452 The attenuation factor (9) for the Parzen smoother is therefore

$$c_{\lambda_c} \approx \frac{2\Delta x}{\lambda_c} \quad (12)$$

453 The value of the integral (11), and thus the attenuation factor (9), are very similar for other
 454 smoothers when the parameters of the smoother are calibrated to give the same half-power filter
 455 cutoff wavelength λ_c .

456 The solution (12) for c_{λ_c} can be understood qualitatively from consideration of smoothing with
 457 a simple running average. In one dimension with a span of $M\Delta x$ for a grid spacing Δx on which
 458 the measurement noise is uncorrelated, i.e., a grid spacing equal to or larger than the footprint
 459 diameter (see appendix B.1 of C19), a block average of M uncorrelated observations reduces the
 460 noise variance by the well-known factor of M^{-1} . It is shown in appendix A of C19 that the half-
 461 power filter cutoff wavelength for running averages with a span of $M\Delta x$ is given approximately by
 462 $\lambda_c = 2M\Delta x$. The number of points in the block average is thus related to the filter cutoff wavelength

463 by $M = \lambda_c / (2\Delta x)$. The noise variance reduction factor can therefore be expressed in terms of the
 464 filter cutoff wavelength as $M^{-1} = 2\Delta x \lambda_c^{-1}$. This is equivalent to the attenuation factor (12).

465 The wavenumber spectrum of residual noise in estimates of u_g after isotropic 2-dimensional
 466 smoothing is given by the unnumbered equation before Eq. (I.31a) of C19,

$$\bar{S}_{u_g}(l) = \frac{g^2}{f^2} 4\Delta x \Delta y \sigma_h^2 |W_{3pt}(l, \Delta y)|^2 W_{\lambda_c}^2(l) \int_0^{k_N} W_{\lambda_c}^2(k) dk, \quad (13)$$

467 where $W_{3pt}(l, \Delta y)$ is the response function (E2) for along-track 3-point centered differences. This
 468 is similar to its counterpart relation (E1a) between the spectrum $S_{u_g}(l)$ of unsmoothed u_g noise and
 469 the SSH noise standard deviation σ_h^2 , except with the added effects of smoothing in each dimension
 470 appearing on the right side of (13).

471 The wavenumber spectrum of residual noise in estimates of v_g after isotropic 2-dimensional
 472 smoothing is Eq. (I.33a) of C19, which is

$$\bar{S}_{v_g}(l) = \frac{g^2}{f^2} 4\Delta x \Delta y \sigma_h^2 W_{\lambda_c}^2(l) \int_0^{k_N} W_{\lambda_c}^2(k) |W_{3pt}(k, \Delta x)|^2 dk \quad (14)$$

473 where $W_{3pt}(k, \Delta x)$ is the response function for across-track 3-point centered differences analogous
 474 to (E2) but with across-track wavenumber k and grid spacing Δx rather than along-track wavenum-
 475 ber l and grid spacing Δy . This is similar to its counterpart relation (E3a) between the spectrum
 476 $S_{v_g}(l)$ of unsmoothed v_g noise and the SSH noise standard deviation σ_h^2 , except again with the
 477 added effects of smoothing in each dimension appearing on the right side of (14).

478 The expressions (13) and (14) for the spectra of smoothed u_g and v_g noise provide mathematical
 479 explanations for the convergence with increasing filter cutoff wavelength λ_c of the variances of
 480 the residual noise in u_g and v_g for the footprint diameters of 1 km and 2 km that was noted in
 481 section 3 from Fig. 1b. This can be understood intuitively by noting that the spectra (13) and (14)
 482 of smoothed estimates of u_g and v_g noise involve products of the response function for 3-point
 483 centered differences and the filter transfer function of the smoothing with a half-power filter cutoff
 484 wavelength of λ_c . The latter depends only on λ_c and not on the footprint diameter [see Eq. (10) for
 485 the case of the Parzen smoother used in this study], but the response function for 3-point centered
 486 differences differs for the different grid spacings associated with the two footprint diameters. In
 487 particular, the band-pass filtering property of the \sin^2 dependence on the square of the response

488 function (E2) attenuates more of the high-wavenumber variability for the footprint diameter and
 489 grid spacing of 2 km compared with the footprint diameter and grid spacing of 1 km. This
 490 dependence on grid spacing is shown in Fig. H.1 of C19 in the context of finite differences on
 491 sample grids with grid spacings of 1 km and 5 km.

492 For any particular choice of footprint diameter, the band-pass filtering from the response function
 493 for 3-point centered differences is the same for any choice of spatial smoothing. As the half-
 494 power filter cutoff wavelength λ_c of the smoothing is increased, the filter transfer function of the
 495 smoothing attenuates progressively more of the variability at lower wavenumbers. This low-pass
 496 filtering eventually attenuates the variance within the wavenumber band over which the response
 497 functions for 3-point centered differences differ on the sample grid spacings of 1 km and 2 km for
 498 the respective footprint diameters of 1 km and 2 km. The effects of this double filtering can be
 499 seen from Fig. H.2 of C19 in the context of finite differencing on sample grids with spacings of 1
 500 km and 5 km. The convergence of the standard deviations of the residual noise in Fig. 1b for the
 501 footprint diameters of 1 km and 2 km thus occurs because the differences between the response
 502 functions for 3-point centered differences on the two grid spacings become progressively more
 503 attenuated with increased spatial smoothing.

504 The wavenumber spectrum of residual noise in estimates of ζ_g after isotropic 2-dimensional
 505 smoothing is Eq. (I.35b) of C19, which can be written as

$$\begin{aligned} \bar{S}_{\zeta_g}(l) = & \frac{g^2}{f^2} 4\Delta x \Delta y \sigma_h^2 W_{\lambda_c}^2(l) \left[\int_0^{k_N} W_{\lambda_c}^2(k) |W_{3pt}(k, \Delta x)|^4 dk \right. \\ & \left. + 2 |W_{3pt}(l, \Delta y)|^2 \int_0^{k_N} W_{\lambda_c}^2(k) |W_{3pt}(k, \Delta x)|^2 dk + |W_{3pt}(l, \Delta y)|^4 \right]. \quad (15) \end{aligned}$$

506 This expression is much more complicated than its counterpart relation (E4) for the spectrum $S_{\zeta_g}(l)$
 507 of unsmoothed noise in ζ_g . This is because the smoothing and the 3-point centered differencing
 508 affect both terms in the expression (D2) for ζ_g and both of these filtering operations are applied in
 509 both dimensions.

510 It can be noted that both terms in the spectrum (15) of smoothed estimates of ζ_g involve the
 511 product of the response function $W_{3pt}(k, \Delta x)$ for 3-point centered differences and the filter transfer
 512 function $W_{\lambda_c}(k)$ of the smoothing with a half-power filter cutoff wavelength of λ_c . As discussed
 513 above from (13) and (14), the differences between these products for the footprint diameters of 1

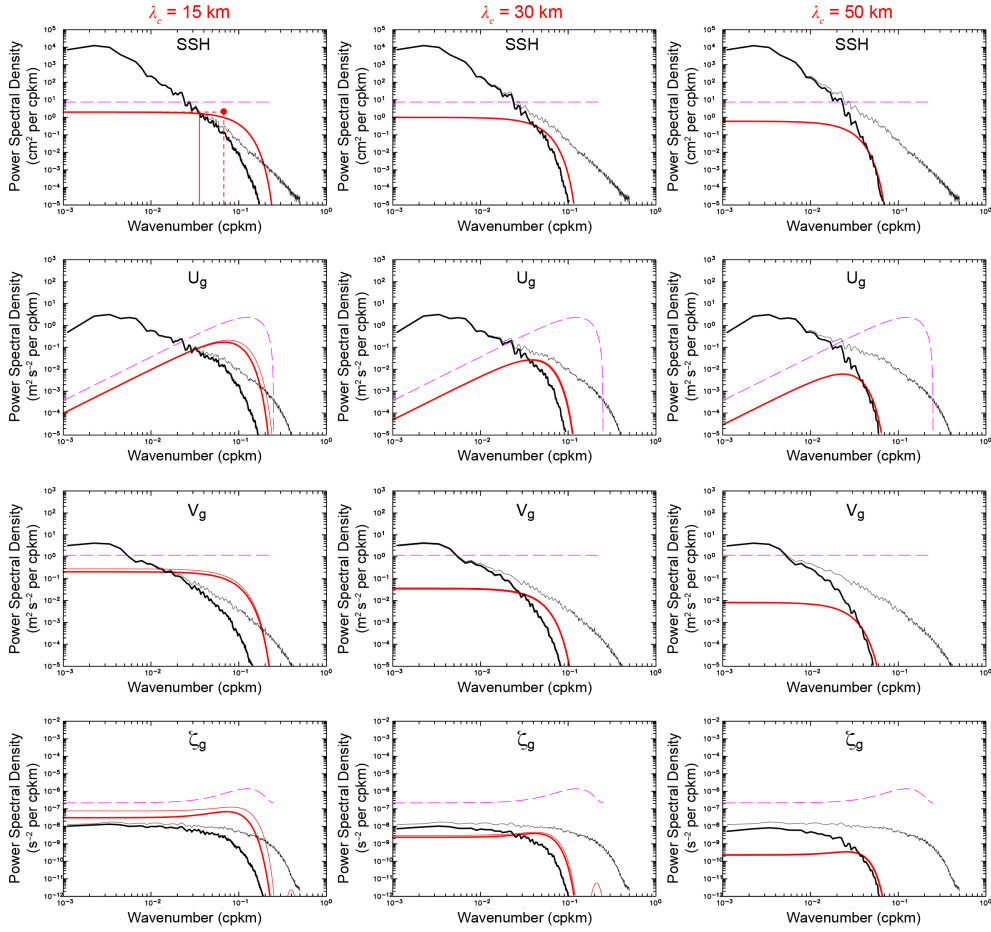
514 km and 2 km decrease with increased filter cutoff wavelength λ_c . This explains the convergence
515 of the standard deviations of the residual noise in Fig. 1c for the footprint diameters of 1 km and 2
516 km.

517 The expressions (8), (13), (14) and (15) are applicable to any low-pass filter with half-power filter
518 cutoff wavelength λ_c , with the caveat that the equivalence of isotropic 2-dimensional smoothing
519 and separate 1-dimensional smoothing in two orthogonal dimensions is less valid for some choices
520 of smoothing operation than for the Parzen smoother used in this study.

522 The spectra of smoothed noise in SSH, u_g , v_g and ζ_g computed from (8), (13), (14) and (15),
523 respectively, are shown in Fig. 2 after applying isotropic 2-dimensional Parzen smoothing to SWOT
524 estimates of SSH for footprint diameters of 1 km and 2 km (thin and thick red lines, respectively)
525 and half-power filter cutoff wavelengths of 15 km, 30 km and 50 km. For reference, the noise
526 spectra from Fig. E1 of unsmoothed variables for the footprint diameter of 2 km that will likely be
527 the SWOT product preferred by most users are shown by the purple dashed lines in each panel. As
528 discussed in appendix A, the choice of $\lambda_c = 15$ km in Fig. 2 corresponds to the filtering applied in
529 the specification of the science requirements for SWOT estimates of SSH. The other two choices
530 of λ_c in this figure illustrate the decrease with increasing λ_c of the spectral power of the noise at all
531 wavenumbers in the SWOT estimates of each variable. The rapid convergence of the noise spectra
532 of smoothed u_g , v_g and ζ_g for the two footprint diameters is also apparent, as was discussed above
533 from (13), (14) and (15) and in section 3 from the standard deviations of the smoothed noise in
534 Figs. 1b and c. Differences between the spectra of smoothed u_g and v_g noise for the two footprint
535 diameters can be seen for $\lambda_c = 15$ km but the two noise spectra are indistinguishable for the cases
536 of $\lambda_c = 30$ km and 50 km. The spectra of smoothed ζ_g noise for the two footprint diameters are
537 barely distinguishable for $\lambda_c = 30$ km but become indistinguishable for the case of $\lambda_c = 50$ km.

538 The distinctions between the wavenumber dependencies of the smoothed noise and the smoothed
539 signals of SSH, u_g , v_g and ζ_g from the model of the California Current System considered in this
540 study (see section 5) can be seen from comparison of the spectra shown by the red and thick black
541 lines, respectively. For reference, the thin black lines are the spectra of the unsmoothed signals.
542 The 2-dimensional smoothing attenuates both the signal and the noise spectra at wavenumbers
543 higher than the filter cutoff wavelength of λ_c^{-1} . The noise spectra for all of the variables are further
544 attenuated progressively more at lower wavenumbers with increasing λ_c . The ζ_g spectrum is also

Wavenumber Spectra for Filter Cutoffs of 15 km, 30 km and 50 km



521 FIG. 2. Swath-averaged wavenumber spectra of smoothed signals (thick black lines) computed in the alongshore
 522 dimension of the model of the California Current System considered here for which descending swaths of SWOT
 523 are approximately parallel to the coast (see Fig. 3) and smoothed noise (red lines) in SWOT estimates of SSH,
 524 velocity components u_g and v_g computed geostrophically from SSH based on the Coriolis parameter f_{37N} for a
 525 latitude of 37°N , and vorticity ζ_g computed from u_g and v_g . The spectra of residual errors after smoothing the
 526 SWOT noise using a Parzen smoother with half-power filter cutoff wavelengths of $\lambda_c = 15$ km, 30 km and 50 km
 527 (columns, left to right) are shown for footprint diameters of 1 km and 2 km (thin and thick red lines, respectively,
 528 which become less distinguishable with increasing λ_c). The horizontal and vertical red dashed and solid lines
 529 and the red dot in the upper left panel are the same as in Fig. E1. For reference, the purple dashed lines are
 530 the spectra of unsmoothed noise for the footprint diameter of 2 km and the thin black lines are the spectra of
 531 unsmoothed signals (see Fig. E1).

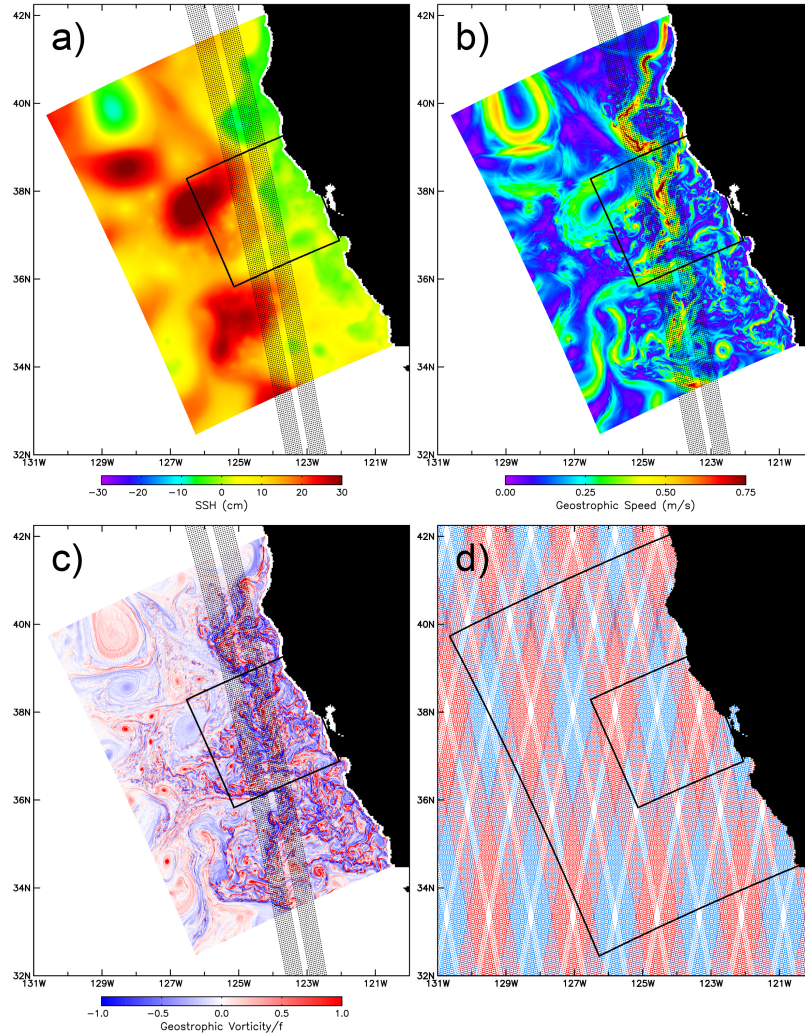
555 somewhat attenuated at lower wavenumbers with increasing λ_c , but much less so than the ζ_g noise
556 spectrum. In all cases, the noise spectra are attenuated much more quickly than the signal spectra
557 with increasing λ_c , thus improving the signal-to-noise ratio. For all four variables, smoothing with
558 a half-power filter cutoff wavelength of at least $\lambda_c = 50$ km is required for the residual noise spectra
559 to become less energetic than the smoothed signal spectra at all wavenumbers.

560 **5. Example maps of simulated noisy SWOT estimates of SSH, velocity and vorticity**

561 A visual assessment of the effects of the statistical characterizations of the noise in sections 2–4
562 on SWOT estimates of SSH and geostrophically computed velocity and vorticity is presented in
563 this section from maps constructed from simulated SWOT data based on the Regional Oceanic
564 Modeling System (ROMS) model of the California Current System (CCS) that was considered by
565 C19. The details of this model are summarized by Molemaker et al. (2015) and in section 2 of
566 C19. The model does not include tides, was forced only by seasonal winds, has a high dissipation
567 that attenuates internal wave variability, and has vertical and horizontal grid resolutions that are
568 not adequate to resolve the full spectrum of internal wave variability. The small-scale features of
569 tides and internal waves are therefore likely underestimated in the model used in this study. The
570 conclusions from the analysis presented here may thus be an overly optimistic assessment of the
571 capabilities for SWOT estimates of velocity and vorticity.

582 An instantaneous snapshot of SSH for the full model domain on the $0.5 \text{ km} \times 0.5 \text{ km}$ grid of the
583 model is shown in Fig. 3a. The speed of the associated geostrophically computed velocity based
584 on the local Coriolis parameter at each grid location is shown in Fig. 3b and the geostrophically
585 computed vorticity normalized by the local Coriolis parameter is shown in Fig. 3c. A descending
586 pair of the parallel swaths from a single simulated overpass of SWOT is overlaid on each of
587 these three maps. This simulated SWOT overpass samples the meandering core of the southward
588 California Current. For reference, the full set of measurement swaths during each 21-day repeat of
589 the SWOT orbit within the bounds of the map is shown in Fig. 3d. The different colors illustrate
590 the 10-day subcycle of the SWOT orbit that is discussed in section 6; the swaths shown in red will
591 be sampled about ten days earlier and ten days later than the swaths shown in blue.

592 To the untrained eye, the submesoscale features that the SWOT mission seeks to observe are
593 difficult to identify in the error-free SSH field in Fig. 3a because the variance of SSH is so small

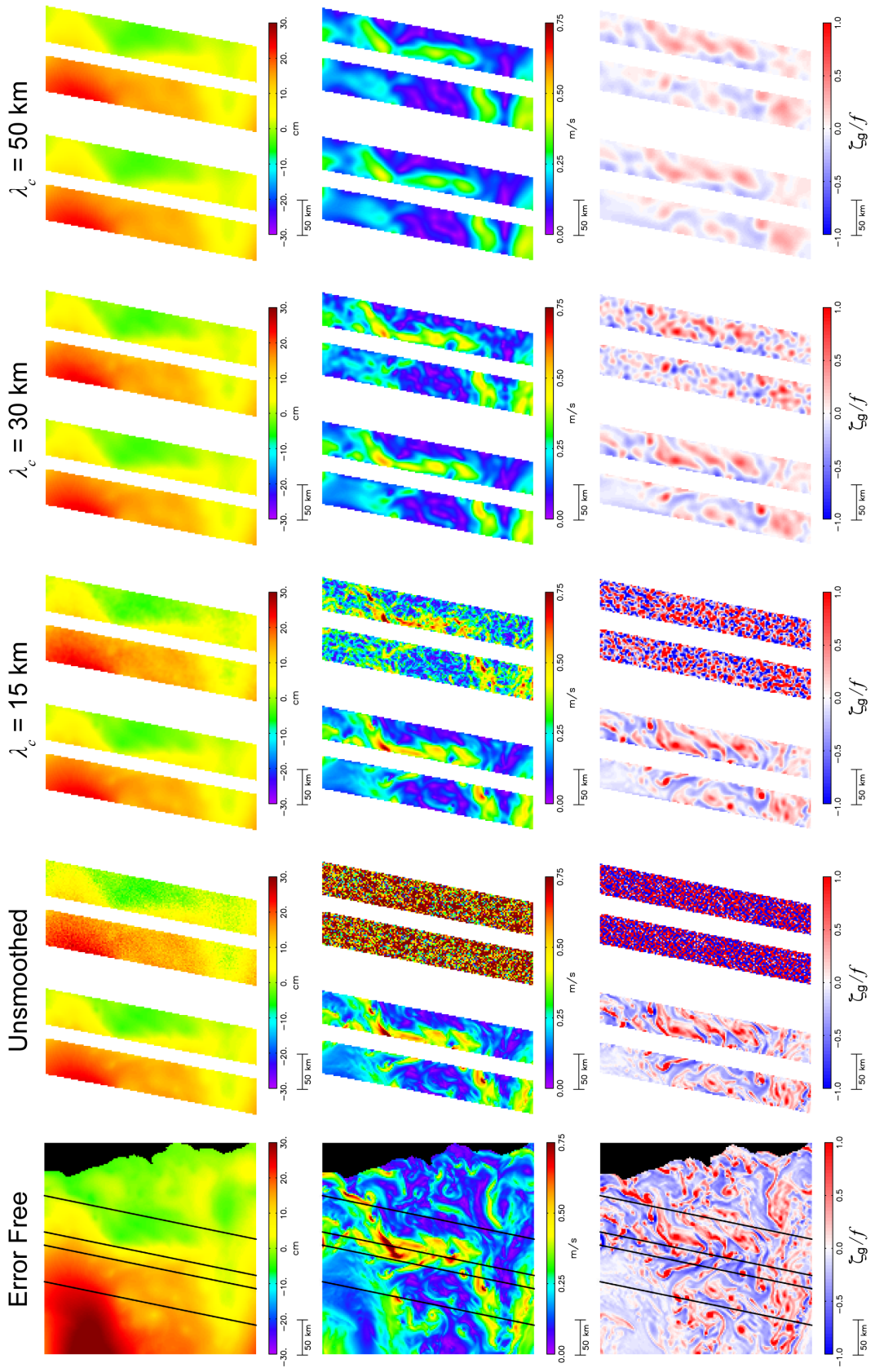


572 FIG. 3. Maps of error-free instantaneous a) SSH; b) the magnitude of geostrophically computed velocity; and
 573 c) the geostrophically computed vorticity for model day 27 May on the $0.5 \text{ km} \times 0.5 \text{ km}$ grid of the model of
 574 the CCS considered here. Panel d) shows simulated SWOT measurement swaths during two 5-day periods that
 575 are separated by 10 days in the 21-day exact repeat SWOT orbit (blue for days 3–8 and red for days 13–18).
 576 The diamond-shaped holes in the sampling pattern in d) are never observed during the 21-day SWOT orbit. The
 577 shaded regions in a)–c) are the pair of simulated SWOT measurement swaths for the single descending overpass
 578 over the CCS model domain that is considered in Figs. 4 and 5. The large box in d) is the full CCS model domain
 579 and the small box in each panel is the subregion of the CCS model that is shown in rotated coordinates in Figs. 4
 580 and 5. The California calibration and validation site for SWOT is centered at 125.4°W , 35.7°N near the bottom
 581 left corner of the small boxes.

594 on scales smaller than 50 km. They are evident as subtle yellow dimples imbedded in the orange
595 and light red areas of the larger mesoscale features in the SSH field. The spatial high-pass filtering
596 from differentiation of the SSH field emphasizes these submesoscale features in the magnitude of
597 the geostrophically computed velocity field shown in Fig. 3b. The submesoscale features are even
598 more emphasized in the geostrophically computed vorticity field in Fig. 3c that was calculated
599 from double differentiation of the SSH field. For the analysis in this study, the simulated SSH
600 fields at the model grid points within the simulated SWOT measurement swaths were used directly
601 without consideration of the differences in location and orientation of the model grid relative to
602 the swath-based grids of the SSH estimates that will be provided by the SWOT Project.

603 To simulate SWOT data, the SSH field in Fig. 3a was smoothed with the half-power filter cutoff
604 wavelength of 4 km that is the minimum filter cutoff for a footprint diameter of 2 km. (As discussed
605 in appendices B and C, the SWOT Project may smooth the SSH with a half-power filter cutoff
606 wavelength somewhat longer than 4 km for the 2 km \times 2 km data product.) The smoothed SSH
607 field on the 0.5 km \times 0.5 km grid of the model was then subsampled on a 2 km \times 2 km grid within
608 the two parallel swaths of the simulated SWOT overpass, thus mimicking the SWOT data product
609 that will likely be preferred by most users. Spatially homogeneous uncorrelated SSH measurement
610 errors with the swath-averaged standard deviation of $\sigma_{2\text{km}} = 1.37$ cm that is derived in appendix
611 C for a footprint diameter of 2 km with 4-km smoothing were added to the gridded values of the
612 model SSH field. The across-swath variations of the measurement noise shown in Fig. C1 and the
613 long-wavelength measurement errors discussed in appendix A are not considered here. Simulated
614 SWOT estimates of velocity and vorticity were computed geostrophically from the error-free and
615 noisy SSH fields with the derivatives approximated as 3-point centered differences.

628 To see the improvement of the signal-to-noise ratio in maps of smoothed SSH, velocity and
629 vorticity constructed from noisy simulated SWOT measurements of SSH, the unsmoothed error-
630 free and noisy SSH fields within only the measurement swaths were smoothed 2-dimensionally
631 using the Parzen smoother with selected choices of half-power filter cutoff wavelength. The residual
632 effects of measurement noise on the smoothed SWOT estimates of SSH, velocity and vorticity are
633 assessed here from consideration of the subregion near the coast in the center of the CCS model
634 domain that is indicated by the small rotated box in each panel of Fig. 3. For reference, the
635 California calibration and validation site for SWOT is centered at 125.4°W, 35.7°N, which is near



616 FIG. 4. Left column (top to bottom): Example maps of instantaneous error-free SSH, the magnitude of
617 geostrophically computed velocity, and geostrophically computed vorticity for model day 27 May within the
618 region of the CCS model shown by the small boxes in Fig. 3. The geostrophic calculations are based on the
619 local Coriolis parameter f at each grid point and the parallel lines in the left panels are the swath edges for
620 the simulated overpass of SWOT shown in Figs. 3a–c. The right four columns show (top to bottom) SSH,
621 geostrophically computed speed and vorticity based only on simulated data within the measurement swaths of
622 the single overpass of SWOT for a footprint diameter of 2 km on a $2\text{ km} \times 2\text{ km}$ grid smoothed using a Parzen
623 smoother with half-power filter cutoff wavelengths of $\lambda_c = 0\text{ km}$ (i.e., unsmoothed), 15 km, 30 km and 50 km.
624 The left pair of swaths in each column shows the smoothed fields without measurement errors and the right pair
625 of swaths includes the effects of spatially homogeneous uncorrelated SSH measurement errors with the standard
626 deviation of $\sigma_{2\text{km}} = 1.37\text{ cm}$ for the footprint diameter of 2 km. The maps have been rotated by a polar angle of
627 24° relative to the latitude-longitude coordinates in Fig. 3 to align with the grid of the CCS model.

636 the bottom left corner of the small rotated boxes. The SSH and geostrophically computed speed
637 and vorticity within this region are shown in the left column of Fig. 4 in rotated coordinates that
638 are aligned with the model grid. These three error-free maps are the same as in the subdomain of
639 the full-resolution maps in Fig. 3, except they have been smoothed and subsampled as summarized
640 above to simulate the SWOT data product with a footprint diameter of 2 km. The edges of the pair
641 of swaths in the simulated single descending overpass of SWOT that are shown in Figs. 3a, b and
642 c are indicated by the parallel lines overlaid on each panel in the left column of Fig. 4.

643 The other four columns in Fig. 4 show the error-free and noisy fields (the left and right pair of
644 swaths in each column) sampled only within the pair of measurement swaths from the simulated
645 SWOT overpass. These four columns correspond to the fields constructed from the simulated
646 SWOT data with smoothing applied based only on SSH observations within the measurement
647 swaths with half-power filter cutoff wavelengths of $\lambda_c = 0\text{ km}$ (i.e., no smoothing), 15 km, 30 km
648 and 50 km. The filter cutoff of 15 km corresponds to the smoothing in the specification of the
649 science requirements for SWOT (see appendix A). According to the criteria proposed in section 5 of
650 C19, the filter cutoffs of 30 km and 50 km correspond approximately to the resolution capabilities
651 of instantaneous maps of geostrophically computed velocity and vorticity, respectively (see Figs.
652 17b and c, Fig. 18 and the top panels of Fig. 51 of C19). Note, however, that the analysis of the

653 resolution capability in instantaneous maps in section 6 of C19 did not take into consideration the
654 edge-effect sampling errors that are discussed below.

655 Consider first the fields constructed from unsmoothed simulated SWOT data that are shown in
656 the second column of Fig. 4. The noise in the SSH measurements is apparent from the speckles
657 in the right pair of swaths. The effects of this visually subtle SSH measurement noise on SWOT
658 estimates of velocity and vorticity completely swamp the submesoscale features in the unsmoothed
659 maps of both of these derivative fields. The noise standard deviations of 0.54 m s^{-1} in each
660 velocity component and $4.9 f$ in the vorticity estimates (see the fourth row in the top half of Table
661 1) are much more energetic because of the amplifications of the effects of SSH measurement noise
662 discussed in appendix D that arise from the finite-difference approximations of the derivatives. It
663 can be inferred from these maps that velocity and vorticity fields will not likely be detectable on any
664 scales from unsmoothed SWOT data, at least in the CCS region considered here, and likely in most
665 regions of the world ocean. Additional smoothing will be required to attenuate the uncorrelated
666 measurement errors and improve the signal-to-noise (S/N) ratio.

667 When the simulated SWOT data are smoothed within the measurement swaths with half-power
668 filter cutoff wavelengths of 15 km, 30 km and 50 km (third, fourth and fifth columns of Fig. 4,
669 respectively), the residual noise diminishes rapidly for all three variables, as shown previously in
670 Fig. 1. The standard deviations of the residual noise in each variable are listed in the bottom
671 half of Table 1. (Note that the residual effects of measurement errors in Table 1 and Fig. 4 do
672 not include the edge-effect sampling errors discussed below that arise from smoothing within the
673 narrow SWOT measurement swaths.) The signals are also attenuated by the smoothing, but not
674 as rapidly as the noise from the effects of uncorrelated measurement errors (see Fig. 3). The S/N
675 ratio thus improves with increased smoothing.

676 For the case of SSH, the residual noise in SWOT estimates of SSH can still be seen with 15-km
677 smoothing from close inspection of the top panel in the third column of Fig. 4. There is no visual
678 evidence of residual SSH noise with filter cutoffs of 30 km or 50 km.

679 For SWOT estimates of velocity, the residual noise is readily apparent in the swath maps with 15-
680 km smoothing shown in the middle panel of the third column of Fig. 4. The most energetic features
681 in the error-free geostrophically computed velocity field with 15-km smoothing in the left pair of
682 swaths can be detected in the noisy field with 15-km smoothing in the right pair of swaths. However,

683 there are numerous features in the 15-km smoothed noisy field that could easily be misinterpreted
684 as signals without the foreknowledge of the details of the error-free smoothed field in the left pair
685 of swaths. The residual velocity noise becomes relatively subtle with the 30-km smoothing in the
686 middle panel of the fourth column of Fig. 4. For the threshold S/N standard deviation ratio of 3.16
687 recommended by C19 (corresponding to a variance ratio of 10), the resolution capability of SWOT
688 estimates of velocity is 32 km. The resolution capability for a more liberal threshold S/N standard
689 deviation ratio of 2 (a variance ratio of 4) is 24 km. Note, however, that the C19 assessments of the
690 resolution capability of instantaneous maps of geostrophically computed velocity do not include
691 consideration of the edge-effect sampling errors that are discussed below.

692 The challenge of estimating vorticity from SWOT data is very apparent from the bottom panels
693 of Fig. 4. Because of the large amplification of the effects of SSH measurement noise from finite
694 difference approximations of the double derivatives required to compute vorticity geostrophically
695 from SSH, the signals are still swamped by the noise with 15-km smoothing. With foreknowledge
696 of the smoothed error-free field in the left pair of swaths in the bottom panel of the fourth column
697 of Fig. 4, the features in the 30-km smoothed error-free geostrophically computed vorticity field
698 can be identified in the 30-km smoothed noisy field in the right pair of swaths. But there are
699 numerous energetic artifacts in the 30-km smoothed noisy field that could easily be misinterpreted
700 as submesoscale features. The residual noise becomes relatively subtle with the 50-km smoothing
701 in the bottom right panel of Fig. 4. The resolution capability of SWOT estimates of instantaneous
702 vorticity deduced by C19 is 54 km based a threshold S/N standard deviation ratio of 3.16 and 44
703 km for a threshold S/N standard deviation ratio of 2. We note again that these assessments of
704 resolution capability by C19 do not take into consideration edge-effect sampling errors.

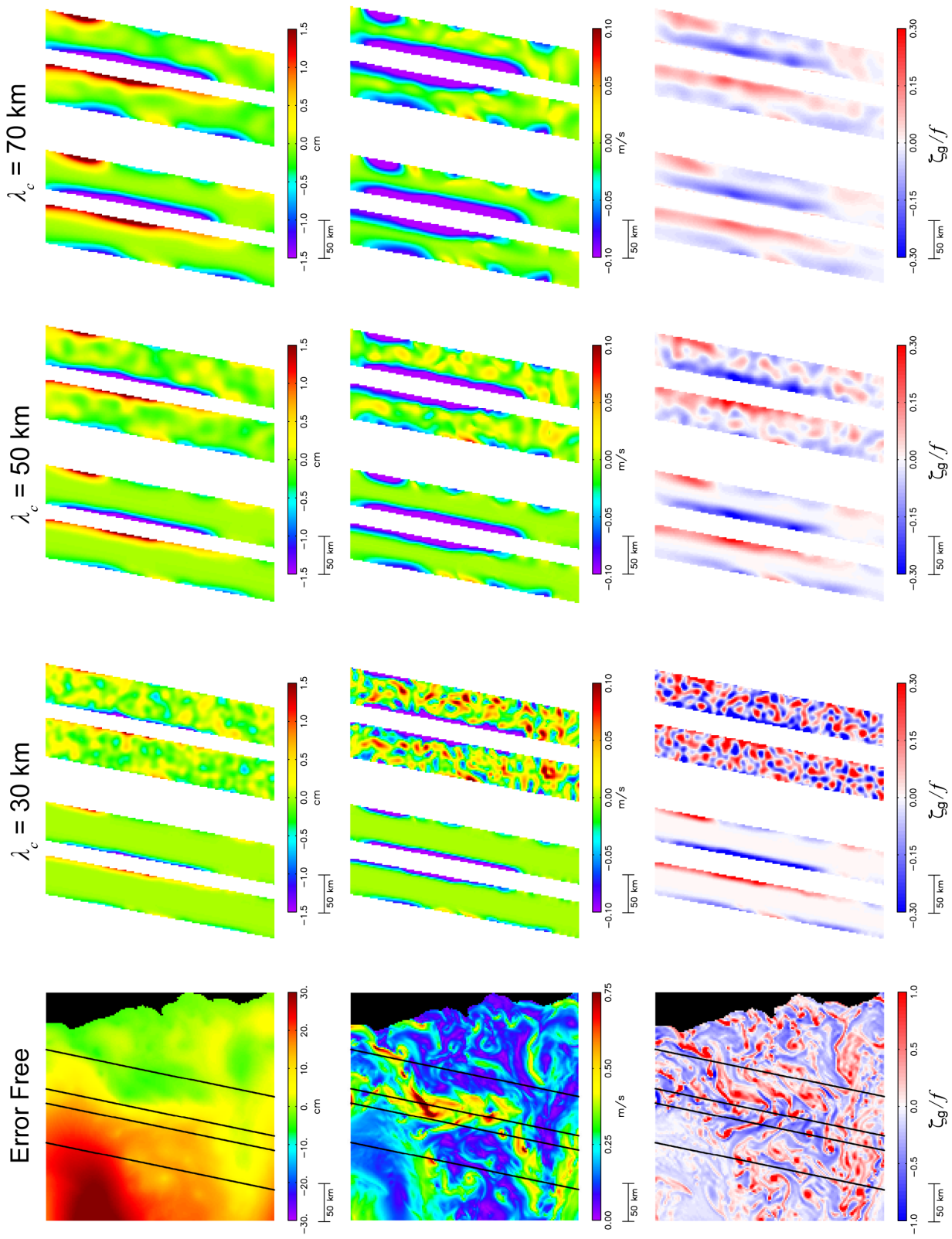
705 The edge-effect sampling errors alluded to above become apparent from the spatial structures of
706 the errors of the simulated SWOT estimates of SSH, velocity and vorticity. This can be achieved
707 for the snapshot fields considered here by subtracting smoothed fields computed from the spatially
708 complete error-free fields in the left column of Fig. 4 from smoothed estimates computed from
709 simulated error-free and noisy SWOT data within just the measurement swaths. For each choice
710 of half-power filter cutoff, these errors can be partitioned into a contribution from sampling errors
711 and a contribution from residual measurement noise. The former corresponds to the errors of the
712 smoothed fields that would be incurred if the smoothing were applied to error-free fields within just

713 the SWOT measurement swaths. For the case considered here in which estimates are constructed
714 from a pair of measurement swaths from a single simulated overpass of SWOT, sampling errors
715 consist only of edge effects of smoothing from incomplete data within the span of the smoother
716 near the edges of the measurement swaths. When the SSH fields are constructed from space-time
717 smoothing of SWOT data from multiple overpasses, sampling errors are also incurred from the
718 discrete and irregular sampling of rapidly evolving small-scale features. This is briefly discussed in
719 section 6 below and is addressed in detail in section 8 of C19. The present analysis considers only
720 the instantaneous fields constructed from simulated SWOT data within the measurement swaths of
721 a single overpass.

722 Maps of the sampling errors and residual measurement noise in smoothed swath estimates of
723 instantaneous SSH, velocity and vorticity are shown in the middle two columns of Fig. 5 for the
724 half-power filter cutoff wavelengths of $\lambda_c = 30$ km and 50 km that were considered in Fig. 4. The
725 right column shows the maps for a larger filter cutoff of $\lambda_c = 70$ km to illustrate the increased edge
726 effects with increased smoothing beyond what was considered in Fig. 4. Note that different color
727 bars are used for all of the error maps in Fig. 5 compared with the color bars for the maps in the
728 left column of Fig. 5 and the color bars for all of the maps in Fig. 4.

739 We focus first on the sampling errors from edge effects in the smoothing of error-free data that
740 are shown in the left pair of swaths in each of the right three columns of Fig. 5. The smoothing
741 in these figures was 2-dimensional and isotropic and was applied based only on data within the
742 two measurement swaths. For estimates at any location across the measurement swath, complete
743 data exist in the along-track dimension. Along the center of the swath, the data in the across-track
744 dimension are symmetrically distributed about the estimation location. The data become more and
745 more asymmetrically distributed as the estimation locations approach the swath edges; complete
746 data exist toward the center of the swath unless the half-span of the smoothing exceeds the distance
747 to the far edge of the swath. Toward the near edge of the swath, however, no data are available
748 beyond the edge of the swath. At the extreme estimation locations along the swath edges, data are
749 available only in the half-plane toward the center of the swath.

750 With large enough half-power filter cutoff wavelength, the estimates in one swath can include
751 some data from the other swath on the opposite side of the 20-km nadir gap. SSH data along
752 the ground track are also available from the nadir altimeter. As discussed in the introduction, the



729 FIG. 5. Left column: The same example maps in rotated coordinates as in Fig. 4 showing (top to bottom)
730 error-free SSH, the magnitude of geostrophically computed velocity and geostrophically computed vorticity. The
731 geostrophic calculations are again based on the local Coriolis parameter f at each grid point and the parallel
732 lines indicate the swath edges for the simulated overpass of SWOT shown in Figs. 3a–c. The right three columns
733 show (top to bottom) the errors of SSH, geostrophically computed speed and geostrophically computed vorticity
734 based only on simulated data within the single overpass of SWOT for a footprint diameter of 2 km on a $2 \text{ km} \times 2$
735 km grid smoothed using a Parzen smoother with half-power filter cutoff wavelengths of $\lambda_c = 30 \text{ km}$, 50 km and
736 70 km . The left pairs of swaths in each column show the edge-effect sampling errors from mapping of error-free
737 fields and the right pairs of swaths include the effects of spatially homogeneous uncorrelated SSH measurement
738 errors with the standard deviation of $\sigma_{2\text{km}} = 1.37 \text{ cm}$ for the footprint diameter of 2 km.

753 very different measurement noise and footprint diameter complicate the merging of nadir altimeter
754 data with the KaRIn estimates of SSH across the two measurement swaths. Data from the nadir
755 altimeter are not considered in this study.

756 Edge effects are visually apparent for all three variables and all three choices of filter cutoff λ_c in
757 the maps in the left pair of swaths in each column of Fig. 5 that were constructed by smoothing error-
758 free simulated data within just the two parallel measurement swaths. With increased smoothing,
759 these edge effects increase in magnitude and extend farther toward the centers of the swaths. For
760 the case of smoothing with a half-power filter cutoff wavelength of $\lambda_c = 70 \text{ km}$, all but a narrow
761 strip along the center of each swath is contaminated by edge effects.

762 For the case of a filter cutoff wavelength of $\lambda_c = 50 \text{ km}$, edge-effect contamination is relatively
763 small within approximately the center half of each swath. This is perhaps surprising since the
764 width of each swath is only 50 km. This can be understood from consideration of the spatial
765 structure of the weighting function of the 2-dimensional Parzen smoother. As discussed in section
766 3, the filtering properties of the Parzen smoother for a given span are very similar to those of
767 the Gaussian smoother with an e-folding scale calibrated to give the same half-power filter cutoff
768 wavelength λ_c as the Parzen smoother (see Fig. C2 in appendix C of C19). The fraction of
769 the Parzen weighting within a given distance of each estimation location can therefore be closely
770 approximated by the fraction of the Gaussian weighting within that distance. An advantage of the
771 latter is that an analytical expression can be derived for the volume of a 2-dimensional Gaussian
772 weighting function within any radial distance from the estimation location. For a 2-dimensional

773 Gaussian function with an e-folding scale of L , the volume within a radius r_i is

$$V_i = \frac{1}{\pi L^2} \int_0^{2\pi} \int_0^{r_i} e^{-(r/L)^2} r dr d\theta = 1 - e^{-(r_i/L)^2}. \quad (16)$$

774 Inclusion of the normalization factor $(\pi L^2)^{-1}$ yields a total volume of $V = 1$ when $r_i = \infty$, thus
 775 assuring that the weighted average is unbiased. The ratio of the volumes within any two radial
 776 distances of r_1 and r_2 from the center of the Gaussian is

$$\frac{V_1}{V_2} = \frac{1 - e^{-(r_1/L)^2}}{1 - e^{-(r_2/L)^2}}. \quad (17)$$

777 The e-folding scale for a Gaussian smoother that has the same half-power filter cutoff wavelength
 778 λ_c as the Parzen smoother is $L = 0.187\lambda_c$ (see appendix C of C19). The weightings for the
 779 Parzen smoother are zero for radial distances larger than a half-span that is related to the filter
 780 cutoff wavelength by $r_{\max} = 0.455\lambda_c$ (see appendix A of C19). We therefore set $r_2 = r_{\max}$, which
 781 corresponds to a volume V_2 that is

$$V_{\max} = 1 - e^{-(r_{\max}/L)^2} = 1 - e^{-(0.455/0.187)^2} = 0.9973$$

782 The Gaussian approximation of the fractional volume of the Parzen smoother within any specified
 783 radius r_1 is therefore

$$\frac{V_1}{V_{\max}} = 1.003 \left[1 - e^{-(r_1/[0.187\lambda_c])^2} \right]. \quad (18)$$

784 The case of a radial distance of $r_1 = \lambda_c/3$, for example, gives a fractional volume of 0.9609. About
 785 96% of the weighting of the Gaussian smoother thus lies within a radial distance of $\lambda_c/3$ from the
 786 estimation location. The exact value for the Parzen weighting determined by numerical integration,
 787 rather than the Gaussian weighting derived analytically above, is about 98%, thus verifying the
 788 close similarity between the Parzen and Gaussian weighting functions. Since virtually all of the
 789 weighting of the Parzen smoother is from data values within a radius of $\lambda_c/3$ it is apparent why
 790 the center half of each swath is not strongly contaminated by edge effects with a filter cutoff of
 791 $\lambda_c = 50$ km. For the case of 70-km smoothing, however, most of the swath is contaminated by edge
 792 effects.

793 The magnitude and extent of contamination by edge effects are very situation specific. They
794 are most severe when there are features near the edges of the swath that have strong gradients in
795 the across-track dimension. Such is the case for the swaths considered in Fig. 5 that straddle the
796 meandering core of the southward California Current. Edge effects will be less pronounced in
797 more quiescent regions where lateral gradients are weaker such as in the offshore region of the
798 model domain shown in Fig. 3.

799 The right pair of swaths in each column in Fig. 5 show the combined effects of sampling errors
800 and residual measurement noise. The latter is manifest as the mottled features in the smoothed
801 error fields that diminish in magnitude with increasing filter cutoff wavelength λ_c . With 30-km
802 smoothing, the total error field is dominated by residual measurement noise for all three variables.
803 For the region considered in Fig. 5, sampling errors from edge effects become larger than the
804 residual measurement noise with 50-km smoothing. The total error fields for all three variables
805 are almost completely dominated by sampling errors from edge effects with 70-km smoothing.

806 We emphasize again that the maps in Figs. 4 and 5 were constructed from simulated SWOT
807 data with homogeneous SSH measurement noise with the swath-averaged standard deviation of
808 $\sigma_{2\text{km}} = 1.37$ cm. The errors near the edges of the swaths will be exacerbated by the larger
809 measurement errors toward the swath edges (see Fig. C1) that have not been considered in this
810 study. Edge-effect sampling errors are therefore likely to be larger from actual SWOT data than
811 inferred from the analysis presented here.

812 **6. Summary and conclusions**

813 The Ka-band Radar Interferometer (KaRIn) on the Surface Water and Ocean Topography (SWOT)
814 satellite with a target launch date in November 2022 promises to revolutionize satellite altimetry
815 by providing high-resolution and accurate measurements across a pair of 50-km swaths separated
816 by a 20-km nadir gap. The primary oceanographic goal of the SWOT mission is to resolve SSH
817 variability on wavelengths longer than about 15 km, which is nearly a factor of five better than can
818 presently be achieved from along-track measurements by conventional nadir-viewing altimeters
819 (Xu and Fu 2012), and more than an order of magnitude better than the resolution capability of
820 SSH fields constructed from measurements by multiple nadir-viewing satellite altimeters (Chelton
821 et al. 2011; Ballarotta et al. 2019). An especially exciting aspect of the SWOT mission is that

822 the swath measurements by KaRIn will provide 2-dimensional views of instantaneous SSH fields.
823 This offers the first opportunity to obtain satellite-based estimates of instantaneous surface velocity
824 and relative vorticity computed geostrophically from the gridded SSH measurements across the
825 two parallel measurement swaths.

826 One of the goals of this study was to determine the standard deviations of the uncorrelated SSH
827 measurement noise for footprint diameters of 0.5 km, 1 km and 2 km (appendix C) from the spectral
828 specification of the science requirement for KaRIn (appendix A), and to quantify the effects of
829 the uncorrelated SSH measurement errors on the noise in geostrophically computed velocity and
830 vorticity (appendix D). We did not address the errors in the geostrophic approximation (see, for
831 example, the discussion in section 3 of C19). Nor did we consider the effects of the long-wavelength
832 measurement errors (see appendix A).

833 Our analysis also considered only the effects of swath-averaged uncorrelated errors in the SSH
834 measurements for a significant wave height (SWH) of 2 m. We did not account for the increases
835 of the measurement errors toward both edges of each measurement swath or the increase of
836 measurement errors with increasing SWH (see Fig. C1). The conclusions of this study are
837 therefore likely somewhat optimistic assessments of the resolution capabilities of SWOT estimates
838 of SSH, velocity and vorticity.

839 The equations in appendices C–E and sections 3 and 4 for the standard deviations and wavenumber
840 spectral characteristics of the noise in these three variables are all expressed in terms of the
841 SSH standard deviation σ_h that is the fundamental characterization of the uncorrelated SWOT
842 measurement errors for the chosen footprint diameter. They can therefore be applied for any location
843 across the measurement swath and any SWH, based on the corresponding standard deviation of
844 the SSH measurement noise at that location. Moreover, the pre-launch estimates of σ_h derived in
845 appendix C for the three footprint sizes considered in this study can be replaced in the equations in
846 appendices C–E and sections 3 and 4 with actual values determined after launch from in-orbit data,
847 or with smaller values that may be obtained in the future through improvements in the onboard and
848 ground-based processing of SWOT data.

849 The analysis in appendix C first considered KaRIn data with the original planned footprint
850 diameter of 1 km on a 1 km \times 1 km grid and then considered the recently revised plan for KaRIn
851 data products with footprint diameters of 0.5 km on an oversampled 0.25 km \times 0.25 km grid and

852 2 km on a 2 km \times 2 km grid (JPL Internal Document 2020). The standard deviations of the
853 SSH estimates with these three footprint diameters were derived from the science requirement for
854 SWOT, which is expressed in a non-conventional form in terms of the wavenumber spectrum after
855 smoothing with a half-power filter cutoff wavelength of 15 km (see appendix A). Because of the
856 large 5.48-cm standard deviation of the SSH measurement noise with the footprint diameter of 0.5
857 km and the large data volume on the 0.25 km \times 0.25 km grid, the vast majority of users will likely
858 prefer the SWOT data product with a footprint diameter of 2 km on a 2 km \times 2 km grid. The noise
859 standard deviation of these SSH estimates will be $\sigma_{2\text{km}} = 1.37$ cm if this data product is produced
860 by smoothing the high-resolution SWOT data product with a half-power filter cutoff wavelength
861 of 4 km (see the discussion in appendices B and C). The smaller footprint size was therefore not
862 considered in our analysis of smoothed simulated SWOT estimates of SSH, velocity and vorticity
863 in sections 3–5.

864 The standard deviations of the noise in SWOT estimates of velocity and vorticity computed
865 geostrophically from SSH with the three footprint diameters of 0.5 km, 1 km and 2 km were
866 derived by propagation-of-error analysis in appendix D. The SWOT estimates of SSH, velocity
867 and vorticity with a chosen footprint diameter are produced by smoothing the raw SWOT data
868 with a half-power filter cutoff wavelength that is twice the footprint diameter. The resulting fields
869 for any choice of footprint diameter are referred to here as “unsmoothed” to distinguish them
870 from the estimates obtained in sections 3–5 with additional 2-dimensional smoothing applied in
871 post-processing. Equations for the wavenumber spectral distributions of the noise variance of
872 unsmoothed SWOT estimates of SSH, velocity and vorticity are presented in appendix E. The
873 effects of SSH noise are amplified by the finite difference approximations of the derivatives in
874 the equations (D1a) and (D1b) for geostrophically computed velocity and the equation (D2b) for
875 vorticity. The amplification of the effects of SSH measurement noise is much greater for vorticity
876 because it consists of the sum of two terms, both of which involve double differentiation of SSH.
877 Mapping the geostrophically computed surface vorticity field from SWOT data will therefore be
878 much more challenging than mapping the SSH and geostrophically computed surface velocity
879 fields.

880 As summarized in section 2, the conclusion from the analysis in the appendices is that the noise in
881 instantaneous maps of all three variables constructed from unsmoothed SWOT data will be too large

882 for any of the SWOT data products to be used directly for most applications. This is acknowledged
883 in the science requirements for KaRIn that are based on smoothing with a half-power filter cutoff
884 wavelength of $\lambda_c = 15$ km to improve the signal-to-noise (S/N) ratio in SWOT estimates of SSH.
885 It was shown in section 3 that the residual noise decreases rapidly with increased smoothing. The
886 noise standard deviations for SSH, velocity components and vorticity decrease as approximately
887 λ_c^{-1} , λ_c^{-2} and λ_c^{-3} , respectively (see Fig. 1). Equations for the wavenumber spectral characteristics
888 of the smoothed noise in each of the three variables are presented in section 4.

889 While smoothing with a half-power filter cutoff wavelength of $\lambda_c = 15$ km may yield an adequate
890 S/N ratio for SSH, the velocity and vorticity computed geostrophically from in-swath SWOT
891 data will likely have to be smoothed with filter cutoff wavelengths of about 30 km and 50 km,
892 respectively. Visual assessments of the effects of this smoothing were presented in section 5
893 from maps of instantaneous estimates of SSH, velocity and vorticity constructed from simulated
894 SWOT data based on a high-resolution numerical model of the California Current System. This
895 simulated SWOT sampling provides insight into the contamination of smoothed estimates of the
896 three variables from edge effects of the smoothing within the 50-km width of each measurement
897 swath. These edge effects arise from incomplete data within the span of the smoother. They will be
898 compounded by the larger measurement noise toward the swath edges that were not considered here
899 (see Fig. C1). Our assessment of SWOT capabilities may therefore be somewhat optimistic. The
900 measurement noise decreases with increased smoothing but the errors from edge effects worsen.
901 Smoothing of the in-swath data will likely have to be limited to a half-power filter cutoff wavelength
902 of about 50 km. Even then, edge effects will likely be too large except within approximately the
903 center half of each 50-km swath. The estimates in this portion of the swath will nonetheless
904 yield important new insight into global mesoscale variability, especially for the smoothed SWOT
905 estimates of vorticity.

906 The analysis here considered only spatial smoothing of in-swath instantaneous SWOT data to
907 improve the S/N ratio. Intuitively, edge effects and measurement errors can be reduced with space-
908 time smoothing from multiple SWOT overpasses of the region of interest. In practice, however,
909 the space-time sampling pattern of the SWOT orbit is not well suited to reducing the errors by
910 time-averaging. The 21-day exact-repeat orbit consists of two subcycles of about 10 days. During
911 each 21-day period, the sampling consists of an interleaved pattern of measurement swaths in

912 which adjacent swaths are sampled 10 days apart (see Fig. 3d; see also Figs. 21 and 22 of C19 and
913 the related discussion in the text of that paper). This sampling pattern introduces a second source
914 of sampling errors that arises from the unresolved rapid evolution of small-scale features during
915 the 10-day time separation between adjacent swaths. While space-time smoothing will be useful
916 for mapping mesoscale variability in SSH (see section 12 of C19), it is shown in section 8 of C19
917 that the resolution capabilities of SWOT estimates of velocity and vorticity actually worsen with
918 time averaging because of sampling errors from the unresolved variability, at least for the time
919 averages of 4 and 14 days considered in that study. Mapping of the surface velocity and vorticity
920 fields from SWOT data will likely have to be done with the aid of dynamic interpolation from a
921 data assimilation model, as suggested, for example, by Ubelmann et al. (2015).

922 The need to smooth SWOT data with a half-power filter cutoff wavelength of 30–50 km for
923 estimates of velocity and vorticity will be disappointing to investigators interested in smaller sub-
924 mesoscale variability. It should be kept in mind that this is much better than the approximate 200-km
925 resolution limitation of the SSH fields constructed from measurements by multiple nadir-viewing
926 altimeters. SWOT data will undoubtedly provide important new insight into ocean dynamics at
927 the short end of the range of mesoscale variability and the long end of the range of submesoscale
928 variability. It is also noteworthy that recent modeling and observational studies suggest that the
929 variability of SSH from which velocity and vorticity will be computed geostrophically from SWOT
930 data may be dominated by baroclinic tides and internal waves on wavelength scales up to 50 km
931 or more (e.g., Rocha et al., 2016; Qiu et al. 2017; 2018; Callies and Wu 2019). SWOT data
932 will undoubtedly provide new insight into the SSH structures of these ageostrophic processes. It
933 may be challenging to separate baroclinic tides and internal wave variability from some of the
934 geostrophic submesoscale signals of interest. The resolution of these other processes in SWOT
935 data may therefore prove to be comparable to the resolution limitations that are imposed by the
936 measurement noise that was the focus of this study.

937 *Acknowledgments.* This research was supported by NASA Grant NNX16AH76G. We thank Jörn
938 Callies, Curtis Chen, Emmanuel Cosme, Lee-Lueng Fu, Sarah Gille, Rosemary Morrow, Ernesto
939 Rodríguez and Nathalie Steunou for comments and suggestions on an earlier version of appendix
940 A and C of this paper that was posted as a white paper on the SWOT website (Chelton 2019).

941 We also thank two anonymous reviewers for helpful and constructive comments that improved the
942 manuscript.

943 *Data availability statement.* The snapshot SSH field from the model of the California Current
944 System that was analyzed for Figs. E1 and 2–5 was obtained from Jeroen Molemaker at the
945 University of California at Los Angeles.

946 APPENDIX A

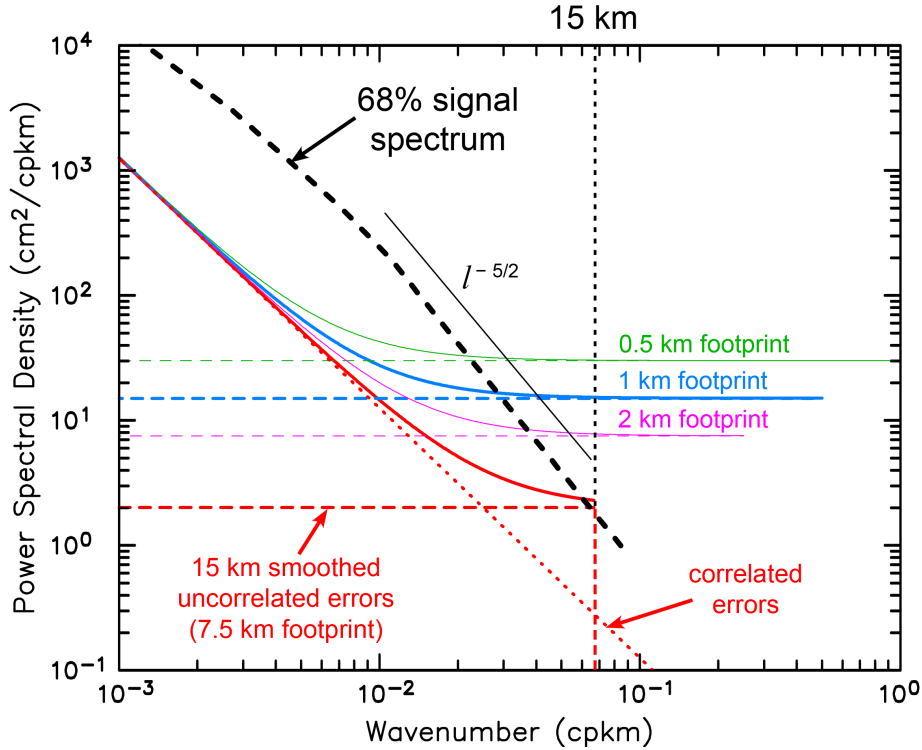
947 **The science requirements for SWOT measurement errors over oceans**

948 The errors of SWOT measurements of SSH can be partitioned into a contribution from uncor-
949 related measurement errors and a contribution from long-wavelength errors attributable to orbit
950 height errors, antenna pointing errors, errors in biases from significant wave height effects, and
951 errors in the corrections for various geophysical effects on the range estimates. Detailed discus-
952 sions of these long-wavelength errors can be found in the Mission Performance and Error Budget
953 document (JPL Internal Document 2017a). As specified in the Science Requirements Document
954 (JPL Internal Document 2018) and various other SWOT documents, the science requirement for
955 the swath-averaged along-track wavenumber spectrum of the long-wavelength errors is

$$S_{red}(l) = 0.0125 l^{-2} \text{ cm}^2/\text{cpkm}, \quad \text{for } 1/1000 < l < 1/15 \text{ cpkm}, \quad (\text{A1})$$

956 where l is the along-track wavenumber. For reasons discussed below, the SWOT documentation
957 does not specify this “red noise” spectrum for wavenumbers higher than $l = 1/15$ cpkm (i.e.,
958 wavelengths shorter than $\lambda = l^{-1} = 15$ km). The spectrum (A1) of long-wavelength errors is shown
959 extrapolated to wavenumbers higher than $l = 1/15$ cpkm by the red dotted line in Fig. A1.

972 The details of the wavenumber spectrum of uncorrelated measurement errors depend on the
973 smoothing applied to the SWOT interferograms by the onboard processor for the gridded SSH
974 data products derived from the interferograms in ground-based processing (see appendix B). The
975 original plan for the gridded SSH data product was to smooth the interferograms to achieve a
976 footprint diameter of 1 km sampled on a $\Delta x \times \Delta y = 1 \text{ km} \times 1 \text{ km}$ grid (JPL Internal Document
977 2017b). The along-track wavenumber spectrum of the uncorrelated measurement errors for a
978 footprint diameter of 1 km is assumed in this study to be constant for all wavenumbers (“white”)



960 FIG. A1. The swath-averaged along-track wavenumber spectra derived from the science requirements. The
 961 dotted red line is the science requirement (A1) for red noise from orbit errors and long-wavelength measurement
 962 errors. The dashed red line is the science requirement (A2) for residual uncorrelated errors after smoothing with
 963 a half-power filter cutoff wavelength of $\lambda_c = 15$ km. The solid red line is the sum of the spectra of the red noise
 964 and the 15-km filtered uncorrelated errors. The dashed blue line is the spectrum (C1) derived in appendix C from
 965 (A2) for the uncorrelated errors in SWOT measurements of SSH for a footprint diameter of 1 km without the
 966 15-km smoothing. The solid blue line is the sum of the red noise spectrum and the white noise spectrum for 1-km
 967 footprint diameter. The green and purple lines are the analogous spectra of uncorrelated errors and total errors for
 968 the footprint diameters of 0.5 km and 2 km, shown for wavenumbers up to their associated Nyquist wavenumbers
 969 of 1 cpkm and 0.25 cpkm for, respectively, the sample grids of $0.5 \text{ km} \times 0.5 \text{ km}$ and $2 \text{ km} \times 2 \text{ km}$ on which the
 970 white noise is uncorrelated for these two footprint diameters. The black dashed line is the 68th-percentile SSH
 971 signal power spectral density from JPL Internal Document (2018).

979 up to the Nyquist wavenumber $l_N = (2\Delta y)^{-1} = 0.5$ cpkm, as shown by the blue dashed line in
 980 Fig. A1 that is derived in appendix C from the science requirements below. The green and purple
 981 dashed lines are the white noise spectra for footprint diameters of 0.5 km and 2 km, which are also

982 derived in appendix C with the assumption that the spectra are white up to the respective Nyquist
 983 wavenumbers of 1 cpkm and 0.25 cpkm. The fixed grids on which the SSH estimates are to be
 984 provided will be geolocated within the nominal measurement swaths of the satellite overpasses of
 985 the 21-day exact-repeat orbit of SWOT. The grid axes will be aligned locally in across-track and
 986 along-track coordinates (x and y , respectively).

987 The goal of the SWOT mission is for KaRIn to resolve SSH on wavelength scales down to 15 km
 988 according to the 68th percentile of the distribution of global wavenumber spectra of SSH inferred
 989 from along-track nadir altimeter data that resolve variability down to a wavelength of about 70 km
 990 (Xu and Fu 2012). The 68th percentile spectrum obtained in this manner was extrapolated from
 991 70 km down to the wavelength of 15 km and is shown by the black dashed line in Fig. A1. The
 992 science requirement for the uncorrelated white noise measurement errors from KaRIn is specified
 993 in the SWOT documentation in a non-conventional form in terms of the swath-averaged along-track
 994 wavenumber spectrum of residual errors after smoothing in post-processing with a half-power filter
 995 cutoff wavelength of $\lambda_c = 15$ km,

$$\bar{S}_{white}(l) = 2 \text{ cm}^2/\text{cpkm}, \quad \text{for } 1/1000 \leq l \leq 1/15 \text{ cpkm.} \quad (\text{A2})$$

996 The overbar signifies the 15-km smoothing of the SWOT data. It can be noted that smoothing with
 997 a 15-km filter cutoff is effectively equivalent to smoothing to a footprint diameter of 7.5 km.

998 The residual white-noise spectrum (A2) after 15-km smoothing of SWOT data, which is shown
 999 by the horizontal red dashed line in Fig. A1, was adopted because it intersects the 68th percentile
 1000 SSH spectrum at the wavelength of 15 km shown by the vertical red dashed line in Fig. A1. The
 1001 15-km smoothing may also be necessary to suppress sources of measurement errors such as wave
 1002 aliasing and spacecraft vibrations that could result in spectral peaks at wavelengths shorter than
 1003 15 km. For the analysis in appendices C–E and sections 3–5, we take (A2) to be the spectral
 1004 characterization of the pre-launch estimate of KaRIn SSH measurement noise. The spectrum (A2)
 1005 could be computed from the SWOT estimates of SSH with 15-km smoothing applied on the swath-
 1006 based grids for any of the three footprint sizes of 0.5 km, 1 km or 2 km considered in appendix
 1007 C.

1008 As in the case of the spectrum (A1) of long-wavelength errors, the SWOT documentation does not
 1009 specify the spectrum (A2) of 15-km smoothed uncorrelated measurement errors for wavenumbers

1010 higher than $l_c = \lambda_c^{-1} = 1/15$ cpkm. If the spectrum of the noise without the 15-km smoothing is
1011 white up to the Nyquist wavenumbers in both dimensions, and if the 15-km smoothing is applied
1012 only 1-dimensionally in the across-track dimension, the along-track spectrum of $\bar{S}_{white}(l)$ would
1013 have the value (A2) for all wavenumbers l up to the Nyquist wavenumber, which is 0.5 cpkm for the
1014 along-track grid spacing of $\Delta y = 1$ km and a footprint diameter of 1 km in the original plan for the
1015 SSH fields generated from SWOT data. If the 15-km smoothing is applied 2-dimensionally with
1016 a realizable filter as suggested in section 2.7.2.a of JPL Internal Document (2018), imperfections
1017 of the filter transfer function would result in attenuation but not complete elimination of the along-
1018 track spectrum (A2) at high wavenumbers, and there would be a gradual rolloff of attenuation
1019 through the half-power filter cutoff wavelength of l_c (see, for example, the red solid line in the
1020 upper left panel of Fig. 2). Note, however, that subsampling the 2-dimensionally smoothed SWOT
1021 data with footprint diameters of 0.5 km, 1 km or 2 km at along-track intervals of 7.5 km would
1022 yield the truncated error spectrum shown by the red dashed line in Fig. A1 if the spectrum
1023 of SSH noise without the 15-km smoothing is white at wavenumbers $l > l_c$, a range that is not
1024 explicitly constrained by the spectral characterizations (A1) and (A2) of the science requirements.
1025 Subsampling at 7.5-km intervals is not specified in the science requirements for SWOT.

1026 It is evident from the extrapolated spectrum shown by the red dotted line in Fig. A1 that
1027 the specification (A1) for long-wavelength measurement errors should have very little power at
1028 wavenumbers higher than $l_c = 1/15$ cpkm. Smoothing with a half-power filter cutoff wavelength
1029 of $\lambda_c = 15$ km would thus have little effect on the long-wavelength errors. The spectrum of the
1030 total measurement errors in 15-km smoothed SWOT data would therefore consist essentially of
1031 the sum of the contributions (A1) and (A2), which is shown by the solid red line in Fig. A1.
1032 This spectrum of the total errors intersects the 68th percentile of the globally distributed SSH
1033 spectra at a wavelength of about 15 km, consistent with the goal of the SWOT mission to achieve
1034 a signal-to-noise ratio of 1 at the 15-km wavelength.

1035 This study considers only the contribution of the uncorrelated measurement errors (A2) to the
1036 total errors in KaRIn estimates of SSH and their effects on estimates of velocity and vorticity com-
1037 puted geostrophically from SWOT data. For smoothing with half-power filter cutoff wavelengths
1038 longer than about 50 km, comparison of the spectra (A1) and (A2) as in Fig. A1 suggests that
1039 additional contributions from the long-wavelength correlated errors may become significant for

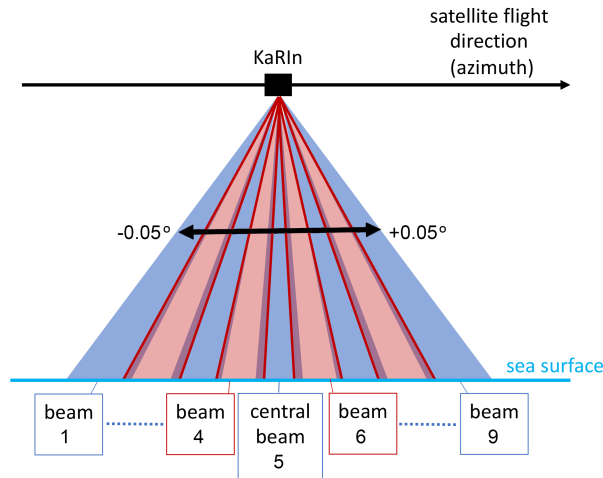
1040 SWOT estimates of SSH. Because of the high-pass filtering of the derivative operator, correlated
1041 SSH measurement errors have a relatively small effect on the SWOT estimates of velocity and
1042 vorticity that are the main focus of this study. The contributions of correlated measurement errors
1043 are therefore not addressed in this study.

1044 APPENDIX B

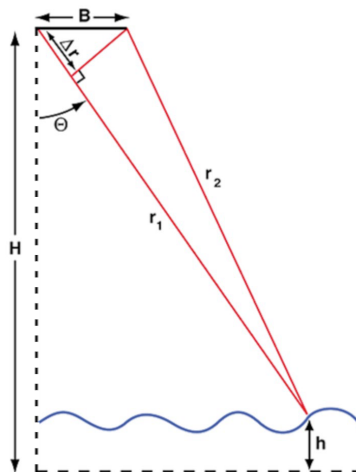
1045 **An overview of onboard and ground-based processing of SWOT data over oceans**

1046 The KaRIn instrument is a synthetic aperture radar (SAR) that uses interferometry to measure
1047 SSH across two 50-km off-nadir swaths with high across-track resolution with SAR processing to
1048 achieve approximately equal along-track spatial resolution over the ocean (JPL Internal Documents,
1049 2017b; 2018). More specifically, KaRIn uses unfocused SAR processing to form nine beams at
1050 slightly different squint angles, fanning out from aft to fore in the along-track direction, with along-
1051 track effective widths of 500 m and offsets of approximately 130 m on the reflecting sea surface.
1052 The angular separation between the fore-most and aft-most beams is approximately 0.1° (Fig. B1).
1053 "Unfocused" processing refers to use of a first-order correction for the range to a point on the sea
1054 surface, and hence the Doppler shift of the returned radar pulse, during the time interval required to
1055 form the synthetic aperture in the along-track direction. "Squinting" refers to the fore-to-aft spread
1056 of the azimuth angles of the synthesized beams formed by the SAR processing. The interferometric
1057 baseline is oriented in the across-track direction, which gives sensitivity to the geometric height of
1058 the targets viewed by each beam.

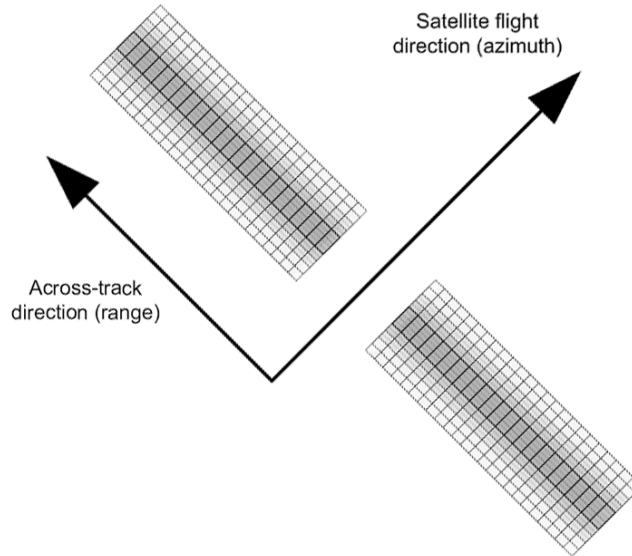
1075 For the interferometry, KaRIn uses two antennas separated by a baseline of $B = 10$ m in the
1076 across-track direction (Fig. B2). A radar pulse is transmitted from one antenna and the reflected
1077 pulse is received by both antennas. The phase difference between the returned radar pulse received
1078 by the two antennas at a known look angle θ gives a measure of the difference Δr in the path lengths
1079 between the reflecting target and each of the two antennas. The height h of the sea surface relative
1080 to a reference surface is estimated from Δr and the height H of the satellite above the reference
1081 surface obtained by precision orbit determination. By processing sequences of returns during short
1082 time windows that carry reflections from different distances ("range-gating"), resolutions of 10 m
1083 at the outer edge of the swath to 70 m at the inner edge can be achieved in the across-track direction.
1084 The phase values as a function of range along each swath of each of the nine fore-to-aft beams



1059 FIG. B1. A schematic depiction of the KaRIn nine-beam measurement geometry, viewed from an across-track
 1060 perspective. For illustration purposes, the fore-to-aft deflection angles of the squinted beams relative to antenna
 1061 boresight are shown with the vertical-to-horizontal aspect ratio reduced by about a factor of 300. The alternating
 1062 blue and pink triangles with slight overlap indicate the nine beams that are measured nearly simultaneously.



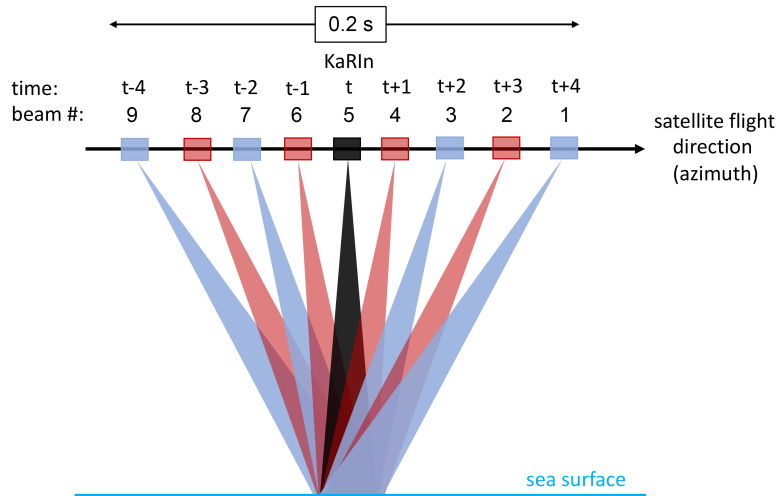
1063 FIG. B2. A schematic description of interferometry. The difference Δr between the path lengths r_1 and r_2 to a
 1064 point on the reflecting sea surface can be determined from the phase difference $\phi = 2kr_1 - k(r_1 + r_2) = k(r_1 - r_2)$,
 1065 where k is the microwave angular wavenumber (equal to 2π over the microwave wavelength) of the radar pulses.
 1066 (After JPL Internal Document 2017a.)



1067 FIG. B3. A plan-view sketch of the nine-beam illumination pattern on the sea surface at a given position of the
 1068 satellite along the ground track. Pulses along the nine SAR beams illuminate nine partly overlapping across-track
 1069 swaths with along-track widths of approximately 500 m and offsets of approximately 200 m. Interferometry
 1070 gives a phase measurement (see Fig. B2) from which SSH is determined with resolution of approximately 500
 1071 m in the across-track direction along each of the nine swaths. The closer spacing of the grid lines are intended to
 1072 depict the oversampling of the across-track interferogram on a 250-m along-track grid, rather than at the 500-m
 1073 across-track spatial resolution of the interferogram. The nadir gap is not shown to scale and only a portion of
 1074 each across-track swath is shown. (Figure courtesy of Gerald Dibarboure.)

1085 forms a two-dimensional gridded interferogram in along-track and across-track coordinates (Fig.
 1086 B3) that is the basis for the KaRIn SSH measurements.

1087 The KaRIn radar transmits with a pulse repetition rate of about 9 kHz, and the onboard processor
 1088 coherently processes a series of nine pulses at each of the nine beam angles to synthesize the
 1089 nine fore-to-aft beams, along each of which across-track interferometric measurements are made.
 1090 Because the nine beams fan out fore-to-aft, they do not view the same along-track position at a given
 1091 time (Fig. B1). As the satellite moves along its ground track, however, pulses transmitted along the
 1092 different beams illuminate a given point on the sea surface at slightly different times (Fig. B4). For
 1093 the KaRIn instrument and SWOT orbit configuration, pulses along all nine beams illuminate a given
 1094 across-track swath within a time period of about 0.2 s, thus resulting in nine nearly simultaneous



1099 FIG. B4. A schematic depiction of the approximate collocation of nine different beams measured by KaRIn as
 1100 the satellite moves along its orbit, viewed from an across-track perspective. The time interval required for the
 1101 nine measurements is approximately 0.2 s. The alternating blue and pink triangles are the same as in Fig. B1,
 1102 except measured at nine different times. The center beam is shown as a black triangle. The vertical-to-horizontal
 1103 aspect ratio has again been reduced by about a factor of 300 for illustration purposes.

1095 across-track interferograms – one each from pulses at different times along each of the nine beams
 1096 – at each measurement point along each across-track grid of the interferogram in Fig. B3. The
 1097 along-track grid points sampled by these nine sets of interferograms are nearly, but not precisely,
 1098 aligned, with spatial offsets of order 10 m in the along-track direction.

1104 As the satellite moves in the along-track direction, the KaRIn instrument thus collects nine
 1105 independent, two-dimensional swaths of data, consisting of nine nearly simultaneous across-track
 1106 interferograms at a sequence of measurement points along the orbit. The natural coordinates for
 1107 these two-dimensional datasets are azimuth (essentially alongtrack) and range (essentially across-
 1108 track). The KaRIN onboard processor smooths each of the nine independent interferograms in
 1109 both the azimuth and range directions with a filter that has a half-power filter cutoff wavelength
 1110 corresponding to a footprint diameter of approximately 0.5 km (JPL Internal Document, 2017b).
 1111 These 0.5-km smoothed interferograms are oversampled on a 0.25 km \times 0.25 km grid and then
 1112 telemetered to ground receiving stations along with ancillary data related to spacecraft navigation

1113 and signal quality (e.g., the radar backscatter amplitude) in a Low-Resolution (LR) dataset for
1114 oceanographic applications. A separate High-Resolution dataset is produced for land hydrology
1115 using different SAR processing techniques.

1116 In ground-based processing, a number of corrections are made to account for instrumental and
1117 geophysical effects. The phase information in the resulting interferograms is then converted to
1118 SSH estimates using auxiliary information such as the spacecraft orientation and position and an
1119 estimate of the mean sea surface. Using the sampling grid of the central beam as a reference,
1120 the SSH estimates from the eight approximately collocated other beams (Fig. B4) are each
1121 spatially interpolated to the measurement locations of the central beam using 2-dimensional sinc
1122 interpolation. At each of the grid points of the central beam, the nine different SSH estimates are
1123 then combined using a maximum likelihood estimator (i.e., a weighted average with a weighting
1124 that is inversely proportional to the noise; see appendix B of JPL Internal Document, 2017b).

1125 The beam-combined SSH estimates with a footprint diameter of 0.5 km are thus obtained on an
1126 approximate $0.25 \text{ km} \times 0.25 \text{ km}$ grid that is referenced to the ground locations of the central beam
1127 of the KaRIn SAR processing, which in turn depends on the spacecraft location and attitude. This
1128 native grid of SSH estimates is interpolated (again using 2-dimensional sinc interpolation) to a
1129 $0.25 \text{ km} \times 0.25 \text{ km}$ Earth-fixed grid that is not aligned with the spacecraft ground track.

1130 A coarser-resolution SWOT SSH product that will be used for most oceanographic applica-
1131 tions will be formed in ground-based processing by isotropic 2-dimensional smoothing of the
1132 $0.25 \text{ km} \times 0.25 \text{ km}$ product on the Earth-fixed grid and subsampling onto a $2 \text{ km} \times 2 \text{ km}$ Earth-
1133 fixed grid. The details of this final smoothing have not yet been decided by the SWOT Project
1134 Office, but it will have a half-power filter cutoff wavelength of at least 4 km.

1135 The net filtering and effective resolution of the SWOT data products on the $0.25 \text{ km} \times 0.25 \text{ km}$ and
1136 $2 \text{ km} \times 2 \text{ km}$ grids are thus determined by the accumulation of the processing steps summarized
1137 above, which include smoothing of interferograms by the onboard processor, interpolation of
1138 eight of the nine smoothed SSH estimates to a common sampling grid, weighted averaging of
1139 those estimates at each of the interpolated grid points, a second interpolation to an Earth-fixed
1140 $0.25 \text{ km} \times 0.25 \text{ km}$ grid, and then a final smoothing in ground-based processing to produce the
1141 $2 \text{ km} \times 2 \text{ km}$ gridded SSH product.

1142 The net filtering of the SSH product on the $2 \text{ km} \times 2 \text{ km}$ grid is dominated by the smoothing in
1143 the final step of the processing. It is shown in appendices C–E and sections 4 and 5 that additional
1144 filtering will be needed in post-processing to suppress the effects of uncorrelated measurement
1145 errors to achieve the residual noise level that is required for most oceanographic applications of
1146 SWOT data. This additional smoothing will ultimately determine the scales of ocean variability
1147 that can be resolved by SWOT. The precise details of the smoothing in the ground-based processing
1148 to obtain the $2 \text{ km} \times 2 \text{ km}$ gridded SSH product are thus of secondary importance. For the analysis
1149 in this study, we have adopted a half-power filter cutoff wavelength of 4 km for the $2 \text{ km} \times 2 \text{ km}$
1150 SSH product; the actual value may end up being somewhat larger than 4 km.

1151 APPENDIX C

1152 **The standard deviations of SWOT measurement noise for three footprint diameters**

1153 The expression (A2) for the uncorrelated measurement errors in terms of their spectral charac-
1154 teristics after applying 15-km smoothing in post-processing is an inconvenient characterization of
1155 measurement noise for the majority of users. It is preferable to know the spectral characteristics
1156 of the uncorrelated measurement errors in the SWOT data without 15-km smoothing in post-
1157 processing. Moreover, a conventional characterization of the uncorrelated measurement errors in
1158 terms of the standard deviation σ_h of the noise at the resolution of the footprint diameter of the
1159 SWOT data is much more useful in practice than a spectral characterization. The two are simply
1160 related by Parseval’s Theorem, which relates σ_h^2 to an integral of the spectrum over wavenumber
1161 [see Eqs. (C2) and (C3) below]. The spectrum of the errors in SWOT estimates of SSH and the
1162 associated standard deviation are derived in appendix F of C19 from the spectral requirement (A2)
1163 for the case of a footprint diameter of 1 km sampled on a $1 \text{ km} \times 1 \text{ km}$ grid. The procedure is
1164 summarized in this section and extended to the cases of footprint diameters of 0.5 km and 2 km
1165 that are in the new plan for the ground-based processing of SWOT data that is summarized in JPL
1166 Internal Document (2020).

1167 For estimation of the along-track wavenumber spectrum of the noisy SWOT measurements of
1168 SSH, smoothing 1-dimensionally with a half-power filter cutoff wavelength of λ_c in the across-track
1169 dimension x attenuates the along-track wavenumber spectrum of uncorrelated measurement errors
1170 at all along-track wavenumbers by the constant factor of c_{λ_c} that is defined by (9) in section 4.

1171 For the Parzen smoother used here, this reduces to (12). This attenuation factor is approximately
 1172 the same for other smoothers when the parameters of the smoother are calibrated to give the same
 1173 half-power filter cutoff wavelength λ_c .

1174 If the smoothing of the SWOT data is instead applied 2-dimensionally and isotropically with an
 1175 ideal (but unrealizable) filter, the additional along-track smoothing would attenuate the spectrum
 1176 to zero at along-track wavenumbers between $l_c = 1/15$ cpkm and the Nyquist wavenumber. For
 1177 a realizable 2-dimensional filter, the spectrum of residual errors after smoothing will exhibit the
 1178 imperfections of a gradual rolloff through the half-power filter cutoff wavenumber l_c , together with
 1179 the higher-wavenumber sidelobes of the realizable filter. The details of these imperfections of the
 1180 filter transfer function are particular to the choice of filter. The result for 2-dimensional filtering
 1181 with a Parzen smoother (see appendix A of C19) are shown by the red solid line in the top left
 1182 panel of Fig. 2. (The sidelobes of the filter transfer function for the Parzen smoother are too small
 1183 to be seen with the dynamic range of the ordinate in this figure – see, for example, Figs. A.1 and
 1184 B.1 of C19.)

1185 For the footprint diameter of 1 km considered in the two versions of the SWOT Science Re-
 1186 quirements Document preceding the current version (JPL Internal Document 2018), and as still
 1187 specified in the current versions of the Mission Performance and Error Budget document (JPL In-
 1188 ternal Document 2017a) and the Onboard Processing and Algorithm Theoretical Basis Document
 1189 (JPL Internal Document 2017b), the grid spacing between samples with uncorrelated measurement
 1190 errors is $\Delta x = \Delta y = 1$ km (see appendix B.1 of C19). With the filter cutoff wavelength $\lambda_c = 15$ km
 1191 of the across-track smoothing in the science requirement specifications for SWOT, the attenuation
 1192 factor (9) that is given by (12) is $c_{\lambda_c} \approx 1/7.5$. An intuitive explanation for the factor-of-2 difference
 1193 between c_{λ_c} and λ_c^{-1} is given in the paragraph following (12) in section 4. The swath-averaged
 1194 white-noise spectrum of uncorrelated SWOT measurement errors obtained from the science re-
 1195 quirement (A2) for the case of a footprint diameter of 1 km without 15-km smoothing would thus
 1196 be a factor of 7.5 times larger than the white-noise spectrum (A2) of the 15-km smoothed SWOT
 1197 data,

$$S_{1\text{km}}(l) = \frac{1}{c_{\lambda_c}} \bar{S}_{white}(l) = \frac{2}{c_{\lambda_c}} \text{cm}^2/\text{cpkm} = 15 \text{cm}^2/\text{cpkm}. \quad (\text{C1})$$

1198 The subscript 1km indicates that (C1) is specific to the case of a footprint diameter of 1 km and
 1199 the omission of an overbar on the left side of the equation implies that no additional smoothing has

1200 been applied to the SWOT data with the 1-km footprint diameter. The white-noise spectrum (C1)
 1201 of SWOT data with a footprint diameter of 1 km is shown by the blue dashed line in Fig. A1.

1202 If the uncorrelated measurement errors are white at wavenumbers higher than $l_c = 1/15$ cpkm,
 1203 the in-orbit performance of SWOT can be more easily validated from the spectrum (C1) of SWOT
 1204 data with 1-km footprint diameter than from the spectrum (A2) that requires 15-km smoothing of
 1205 SWOT data. Furthermore, the white-noise floor of the total error spectrum for a footprint diameter
 1206 of 1 km and a grid spacing of $\Delta y = 1$ km (the solid blue line in Fig. A1) extends far beyond
 1207 the wavenumber $l_c = 1/15$ cpkm to the Nyquist wavenumber of $l_N = 0.5$ cpkm and is thus clearly
 1208 distinguished from the SSH signal spectrum and the red noise spectrum at the higher wavenumbers.

1209 The variance of the uncorrelated measurement errors in the SWOT estimates of SSH with a
 1210 footprint diameter of 1 km and without additional smoothing in post-processing can be obtained
 1211 by Parseval's Theorem that relates the variance σ^2 of a variable to the integral of its spectrum $S(l)$,

$$\sigma^2 = \int_0^{l_N} S(l) dl. \quad (C2)$$

1212 For the case of $S(l)$ equal to the constant white-noise spectrum (C1), this reduces to

$$\sigma_{1\text{km}}^2 = l_N S_{1\text{km}}(l) = \frac{S_{1\text{km}}(l)}{2\Delta y} = 7.5 \text{ cm}^2. \quad (C3a)$$

1213 For M discretely sampled observations at along-track intervals of Δy , this integral becomes a
 1214 discrete summation,

$$\sigma_{1\text{km}}^2 = \sum_{j=1}^{M/2} S_{1\text{km}}(l_j) \Delta l = \frac{M\Delta l}{2} S_{1\text{km}}(l_j), \quad (C3b)$$

1215 where $l_j = j\Delta l$ and $\Delta l = (M\Delta y)^{-1}$ is the Fourier wavenumber interval. The zero wavenumber
 1216 is excluded from the sum in (C3b) because it does not contribute to the sample variance. The
 1217 multiplicative factor on the right side of (C3b) is $M\Delta l/2 = (2\Delta y)^{-1} = l_N$. The right side of (C3b)
 1218 is therefore the same as the right side of (C3a). The swath-averaged standard deviation of the
 1219 uncorrelated measurement errors in SWOT data for a footprint diameter of 1 km derived from the
 1220 science requirement (A2) is the square root of (C3a),

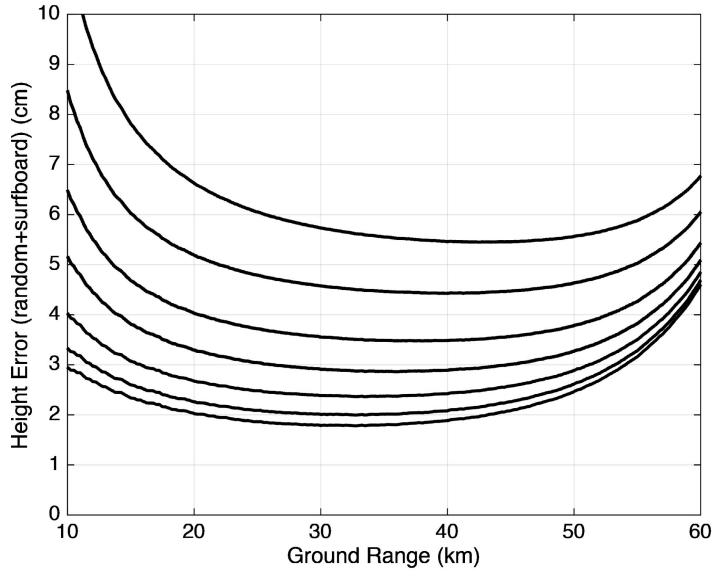
$$\sigma_{1\text{km}} = 2.74 \text{ cm}. \quad (C4)$$

1221 As noted above, this measurement noise is uncorrelated on a sample grid spacing of $1 \text{ km} \times 1 \text{ km}$
1222 for the 1-km footprint diameter considered here.

1223 The value of 2.74 cm for $\sigma_{1\text{km}}$ cannot be found in any of the present SWOT documents. However,
1224 the specification of the white-noise contribution to the total error spectrum in the unnumbered first
1225 equation in section 5.1 of JPL Internal Document (2017a) can be combined with the unnumbered
1226 last equation in section 5.1.1 of that document to deduce a value of $\sigma_{1\text{km}} = 2.74 \text{ cm}$. Somewhat
1227 smaller values of 2.5 cm and 2.4 cm are stated without derivation in sections 5.1.3 and 5.4.5,
1228 respectively. And a value of 2.7 cm is stated without explanation in Fig. 16 of JPL Internal
1229 Document (2017b), albeit with units mislabeled as mm rather than cm. The lower values of
1230 2.5 cm and 2.4 cm may be the projected best estimates of what will actually be achieved on
1231 orbit. Or they may consider only the effects of instrumental errors, neglecting smaller sources of
1232 non-instrumental uncorrelated errors such as the effects of spacecraft pointing errors on the signal-
1233 to-noise ratio across the measurement swaths. Both explanations have been offered in personal
1234 communications with different SWOT Project team members.

1235 The preceding analysis is for the overall average standard deviation of uncorrelated measurement
1236 errors across the SWOT measurement swaths for a footprint diameter of 1 km and a significant
1237 wave height (SWH) of 2 m. In actuality, the errors will be smallest near the middle of each
1238 measurement swath and increase toward both edges of the swaths, and will increase monotonically
1239 with increasing SWH. The projected estimates of the dependencies of the standard deviation of
1240 uncorrelated measurement errors on SWH and across-track swath location x are shown in Fig.
1241 C1 for a footprint diameter of 1 km. The corresponding across-track variation of the white-noise
1242 along-track wavenumber spectral value of the uncorrelated measurement errors can be determined
1243 by inverting (C3a) to obtain $S_{1\text{km}}(l, x, \text{SWH}) = l_{\mathcal{N}}^{-1} \sigma_{1\text{km}}^2(x, \text{SWH})$ based on the measurement error
1244 standard deviation $\sigma_{1\text{km}}(x, \text{SWH})$ shown in Fig. C1 for the SWH and swath location x of interest.

1252 The discussion hereinafter considers only the across-swath average SSH measurement noise
1253 standard deviation for a significant wave height of 2 m. Note, however, that the SWOT simulator
1254 software that is provided by the SWOT Project (JPL Internal Document 2017c) incorporates
1255 estimates of both the across-track variation of uncorrelated measurement errors and the additional
1256 long wavelength, correlated errors discussed in appendix A.



1245 FIG. C1. Estimates of the dependencies of the standard deviation of uncorrelated errors of SWOT measurements
 1246 of SSH on significant wave height (SWH) and swath location relative to the satellite ground track for a footprint
 1247 diameter of 1 km. The seven solid lines correspond to SWH values increasing from 2 m to 8 m at increments of
 1248 1 m (bottom to top). The errors for 0-m SWH are essentially the same as those shown for 2-m SWH. The standard
 1249 deviations of the uncorrelated errors for footprint diameters of 0.5 km and 2 km are, respectively, factors-of-2
 1250 larger and smaller than shown here [see Eqs. (C6) and (C9)]. (Figure adapted from Fig. C1.5 of JPL Internal
 1251 Document 2017c.)

1257 The original plan for ground-based processing of the SWOT data over the oceans to achieve
 1258 the footprint diameter of 1 km that was considered above and by C19 has evolved to a new plan
 1259 to provide the SWOT data with two different footprint sizes (JPL Internal Document 2020). As
 1260 discussed in appendix B, a high-resolution product will be provided with a footprint diameter of
 1261 0.5 km on an oversampled $0.25 \text{ km} \times 0.25 \text{ km}$ grid. In addition, a coarser resolution product will
 1262 be produced from the high-resolution product on a $2 \text{ km} \times 2 \text{ km}$ grid. As noted in appendix B,
 1263 the spatial smoothing to be applied for the $2 \text{ km} \times 2 \text{ km}$ gridded SSH product has not yet been
 1264 finalized by the SWOT Project Office. For the analysis presented here, we will assume that this
 1265 smoothing will be equivalent to a footprint diameter of 2 km. This corresponds to smoothing with
 1266 a half-power filter cutoff wavelength of 4 km, which is the smoothing for which the residual noise
 1267 in the $2 \text{ km} \times 2 \text{ km}$ gridded estimates of SSH is essentially uncorrelated (see appendix B.1 of C19).

1268 As noted in appendix B, the SWOT Project may smooth with a half-power filter cutoff wavelength
 1269 somewhat longer than 4 km, thus resulting in 2 km \times 2 km gridded estimates of SSH that are
 1270 oversampled in the sense that the noise is somewhat correlated between neighboring grid points.
 1271 Since additional smoothing will have to be applied in post-processing by most users (see sections
 1272 3–5), the somewhat greater smoothing that may be applied in the ground-based processing for the
 1273 2 km \times 2 km gridded SSH product would not significantly alter any of the conclusions of this study.

1274 The noise in SSH estimates with the footprint diameter of 0.5 km is essentially uncorrelated on
 1275 a sample grid spacing of 0.5 km \times 0.5 km. The increased noise of measurement errors with the
 1276 footprint diameter of 0.5 km compared with a footprint diameter of 1 km is easily determined from
 1277 the well-known formula that the variance of the average of N uncorrelated measurement errors
 1278 decreases as $1/N$. Since there are $N = 4$ uncorrelated measurements with 0.5-km footprint in each
 1279 1 km \times 1 km area, the variance of the uncorrelated errors with a footprint diameter of 0.5 km is
 1280 four times larger than (C3a),

$$\sigma_{0.5\text{km}}^2 = 4\sigma_{1\text{km}}^2 = 30 \text{ cm}^2. \quad (\text{C5})$$

1281 The swath-averaged standard deviation of the uncorrelated errors with a footprint diameter of
 1282 0.5 km is therefore two times larger than (C4),

$$\sigma_{0.5\text{km}} = 5.48 \text{ cm}. \quad (\text{C6})$$

1283 The recommendation of the SWOT Science Team is to post the high-resolution SSH estimates
 1284 with the footprint diameter of 0.5 km on an oversampled 0.25 km \times 0.25 km grid (JPL Internal
 1285 Document 2020). The variance of the SSH measurement errors for the 0.5-km footprint diameter
 1286 is unchanged on the oversampled grid, but the errors at neighboring 0.25 km \times 0.25 km grid points
 1287 are correlated. The oversampling on a 0.25 km \times 0.25 km grid does not alter the wavenumber
 1288 spectrum of the noise at wavenumbers smaller than the Nyquist wavenumber of $l_N = 1$ cpkm
 1289 associated with the 0.5 km \times 0.5 km grid spacing for uncorrelated errors.

1290 The swath-averaged constant white noise spectrum of the uncorrelated errors for the smaller
 1291 footprint diameter of 0.5 km and the higher Nyquist wavenumber of $l_N = 1$ cpkm associated with
 1292 the grid spacing of $\Delta y = 0.5$ km can be obtained from (C5) by inverting an expression analogous

1293 to (C3a) to get

$$S_{0.5\text{km}}(l) = \frac{1}{l_N} \sigma_{0.5\text{km}}^2 = 30 \text{ cm}^2/\text{cpkm}. \quad (\text{C7})$$

1294 This spectrum is shown by the green dashed line in Fig. A1. It should be noted that the statistics
1295 (C5), (C6) and (C7) for the uncorrelated errors in SWOT estimates of SSH with a footprint diameter
1296 of 0.5 km are not science requirements for SWOT. The only science requirement for uncorrelated
1297 measurement errors is the spectrum (A2) obtained after smoothing the SWOT data 1-dimensionally
1298 in the across-track dimension with a half-power filter cutoff wavelength of 15 km in post-processing.

1299 Because of the large standard deviation (C6) of uncorrelated measurement errors in SSH estimates
1300 with a footprint diameter of 0.5 km and the large data volume for SSH fields on the oversampled
1301 $0.25 \text{ km} \times 0.25 \text{ km}$ grid, the SWOT Project will also provide a lower-resolution and lower-noise
1302 product on a $2 \text{ km} \times 2 \text{ km}$ grid (JPL Internal Document 2020). This product will be preferred for
1303 most oceanographic applications of SWOT data; as shown in sections 3–5, most users will want
1304 to apply additional smoothing. Since there are $N = 16$ measurements with 0.5-km footprint in
1305 each $2 \text{ km} \times 2 \text{ km}$ grid cell, the variance of the uncorrelated SSH measurement errors with the
1306 spatial smoothing equivalent to a footprint diameter of 2 km that is considered here is a factor-of-16
1307 smaller than (C5),

$$\sigma_{2\text{km}}^2 = \frac{1}{16} \sigma_{0.5\text{km}}^2 = 1.875 \text{ cm}^2. \quad (\text{C8})$$

1308 This expression can be equivalently derived from (C3a) and the fact that there are $N = 4$ measure-
1309 ments with 1 km footprint in each $2 \text{ km} \times 2 \text{ km}$ grid cell, resulting in a variance $\sigma_{2\text{km}}^2$ that is a
1310 factor-of-4 smaller than (C3a). The swath-averaged standard deviation of the uncorrelated SSH
1311 measurement errors with a footprint diameter of 2 km is thus a factor-of-4 smaller than (C6) and a
1312 factor-of-2 smaller than (C4),

$$\sigma_{2\text{km}} = 1.37 \text{ cm}. \quad (\text{C9})$$

1313 The standard deviation of the noise in the $2 \text{ km} \times 2 \text{ km}$ SSH product will be slightly smaller than
1314 this if the half-power filter cutoff wavelength applied to the $0.25 \text{ km} \times 0.25 \text{ km}$ SSH product is
1315 longer than the value of 4 km assumed in the analysis above.

1316 The swath-averaged constant white noise spectrum of the uncorrelated errors for the coarser
1317 footprint diameter of 2 km and the lower Nyquist wavenumber of $l_N = 0.25 \text{ cpkm}$ associated with
1318 the grid spacing of $\Delta y = 2 \text{ km}$ can be obtained from (C8) by again inverting an expression analogous

1319 to (C3a) to get

$$S_{2\text{km}}(l) = \frac{1}{l_N} \sigma_{2\text{km}}^2 = 7.5 \text{ cm}^2/\text{cpkm}. \quad (\text{C10})$$

1320 This spectrum is shown by the purple dashed line in Fig. A1.

1321 The SWOT estimates of SSH with the three footprint diameters of 0.5 km, 1 km and 2 km
1322 considered above are produced by smoothing the raw SWOT data with a half-power filter cutoff
1323 wavelength that is twice the footprint diameter (see appendix B.1 of C19). The resulting fields for
1324 any choice of footprint diameter are referred to throughout this study as “unsmoothed” to distinguish
1325 them from the estimates obtained in sections 3–5 with additional 2-dimensional smoothing applied
1326 in post-processing.

1327 It was noted above that the in-orbit performance of the uncorrelated errors in KaRIn estimates
1328 of SSH can be validated more easily from the spectrum (C1) with a footprint diameter of 1 km
1329 and no additional smoothing than it can from the spectrum (A2) of SSH after 15-km smoothing
1330 in post-processing. The SWOT performance can likewise be easily validated from the spectrum
1331 (C7) of gridded SWOT estimates of SSH with a footprint diameter of 0.5 km or from the spectrum
1332 (C10) of SWOT data smoothed to have a footprint diameter of 2 km. It will be much easier to
1333 evaluate the SWOT performance from unsmoothed SSH observations with any of the three footprint
1334 diameters considered above because the white-noise floor of the spectrum of noisy SSH will be
1335 more energetic than both the SSH signal spectrum and the spectrum (A1) of long-wavelength
1336 measurement errors at wavenumbers higher than the upper limit of $l = 1/15$ cpkm in the science
1337 requirement specifications (A1) and (A2). In contrast, the 68th percentile spectrum of SSH with
1338 measurement errors and 15-km smoothing does not asymptote to the white-noise floor (A2) of the
1339 uncorrelated measurement errors at $l = 1/15$ cpkm. These alternative procedures for evaluating the
1340 SWOT performance from data without 15-km smoothing assume that the spectra of the uncorrelated
1341 measurement errors are white for all wavenumbers up to the Nyquist wavenumber l_N associated
1342 with each of the three footprint diameters considered here.

1343 APPENDIX D

1344 **The standard deviations of the noise in SWOT estimates of velocity and vorticity**

1345 The discussion of SSH measurement noise in appendix C considered the effects of footprint
 1346 diameter on the swath-averaged standard deviation of the uncorrelated measurement errors. Many
 1347 SWOT users will be interested in estimates of surface velocity and vorticity computed geostrophically
 1348 from the gridded fields of SWOT estimates of SSH. The equations for the x and y components
 1349 of geostrophic velocity are

$$u_g = -\frac{g}{f} \frac{\partial h}{\partial y} \quad (\text{D1a})$$

$$v_g = \frac{g}{f} \frac{\partial h}{\partial x}, \quad (\text{D1b})$$

1350 where h is the SSH, $g = 9.81 \text{ m s}^{-2}$ is the gravitational acceleration and $f = 2\Omega \sin \theta$ is the Coriolis
 1351 parameter for Earth rotation rate $\Omega = 7.29 \times 10^{-5} \text{ s}^{-1}$ and latitude θ . The relative vorticity computed
 1352 from u_g and v_g or from SSH is

$$\zeta_g = \frac{\partial v_g}{\partial x} - \frac{\partial u_g}{\partial y} \quad (\text{D2a})$$

$$= \frac{g}{f} \left(\frac{\partial^2 h}{\partial x^2} + \frac{\partial^2 h}{\partial y^2} \right). \quad (\text{D2b})$$

1353 The spatial derivatives in (D1) and (D2) must be estimated from the discretely sampled SWOT
 1354 estimates of SSH by finite differences. This finite differencing imposes a filtering operation on the
 1355 SSH fields. The derivative operator for a continuous variable is a high-pass filter with a wavenumber
 1356 dependence of k^2 or l^2 , depending on whether the derivative is in the x or y dimension, respectively.
 1357 However, the 3-point centered difference operator applied to discretely sampled data, which is the
 1358 method used to estimate derivatives in this study, is a band-pass filter with a response function that
 1359 has $\sin^2(2\pi k \Delta x)$ or $\sin^2(2\pi l \Delta y)$ dependence on wavenumber k or l [see Eq. (E2) below].

1360 The expressions for the swath-averaged standard deviations σ_{u_g} and σ_{v_g} of the noise of the
 1361 centered-difference estimates of the geostrophically computed velocity components (D1) and for
 1362 the standard deviation σ_{ζ_g} of the noise of the centered-difference estimate of the vorticity computed
 1363 from the first derivatives of u_g and v_g in (D2a) or from the second derivatives of SSH in (D2b)
 1364 are derived by propagation-of-error analysis in appendix G.1 of C19. The resulting equations are
 1365 expressed in terms of any specified standard deviation σ_h of the SSH measurement errors and the
 1366 grid spacings Δx and Δy of the discretely sampled observations. As discussed below, the effects of

SSH errors on estimates of u_g and v_g are amplified in the finite differencing of SSH. The effects of these errors are further amplified by the additional finite differencing required to estimate ζ_g from u_g and v_g as in (D1a) or directly from SSH as in (D1b). The equations for σ_{u_g} , σ_{v_g} and σ_{ζ_g} are applied in this section for all three of the footprint diameters of 0.5 km, 1 km and 2 km considered in appendix C.

Consider first the noise in the geostrophically computed velocity component v_g . The propagation of uncorrelated SSH measurement errors through the 3-point centered-difference estimates of the geostrophic equation (D1b) for v_g yields a noise variance that can be written in the form

$$\sigma_{v_g}^2 = \frac{g^2}{f^2} \frac{2\sigma_h^2}{4\Delta x^2} \left[1 - \rho_h(2\Delta x) \right], \quad (\text{D3a})$$

where Δx is the sample interval in the x dimension and $\rho_h(2\Delta x)$ is the autocorrelation of the SSH measurement noise at a spatial lag of $2\Delta x$. This is Eq. (G.2) of C19. When the sample interval Δx is equal to or larger than the footprint diameter, the SSH noise at all grid points is essentially uncorrelated and the term $\rho_h(2\Delta x)$ inside the square brackets is negligible. This can be seen from the bottom panel of Fig. B1a of C19 for the case of a footprint diameter of 1 km on a $1 \text{ km} \times 1 \text{ km}$ grid. For smaller sample interval, the SSH errors at neighboring grid points become correlated so that $\rho_h(2\Delta x)$ is nonzero.

The non-reduced form of the ratio that multiplies the terms in square brackets in (D3a) reveals the amplification of the effects of SSH measurement noise by the centered differencing alluded to above. The multiplicative factor $(g/f)^2/(4\Delta x^2)$ arises from a combination of the factor g/f in the geostrophic relation (D1b) and the factor $2\Delta x$ in the denominator of the 3-point centered difference approximation of the derivative in (D1b). These factors transform the units of squared SSH to units of squared velocity component. The remaining factor $2\sigma_h^2$ in the numerator of (D3a) shows the well-known fact that finite differencing of two noisy SSH measurements doubles the SSH noise variance. If the SSH field is oversampled by decreasing Δx relative to the footprint diameter, the noise variance $\sigma_{v_g}^2$ increases because of the smaller factor Δx^2 in the denominator of (D3a). This increase is mitigated to a small extent by the autocorrelation $\rho_h(2\Delta x)$ at lag Δx that becomes nonzero and positive when Δx is smaller than the spacing at which the SSH observations are uncorrelated.

1394 In reduced form, (D3a) becomes

$$\sigma_{v_g}^2 = \frac{g^2}{f^2} \frac{1}{2\Delta x^2} \left[1 - \rho_h(2\Delta x) \right] \sigma_h^2. \quad (\text{D3b})$$

1395 The analogous expression for the variance of the noise in the geostrophically computed velocity
1396 component u_g derived by propagation of the SSH errors through the geostrophic equation (D1a) is

$$\sigma_{u_g}^2 = \frac{g^2}{f^2} \frac{1}{2\Delta y^2} \left[1 - \rho_h(2\Delta y) \right] \sigma_h^2, \quad (\text{D4})$$

1397 where Δy is the sample interval in the y dimension and $\rho_h(2\Delta y)$ is the autocorrelation of the SSH
1398 measurement noise at a spatial lag of $2\Delta y$. For a given SSH noise variance σ_h^2 , it is apparent
1399 from (D3) and (D4) that the noise variances of the geostrophically computed velocity components
1400 decrease with increasing Coriolis parameter f , i.e., with increasing latitude.

1401 For the cases of the three footprint diameters of 0.5 km, 1 km and 2 km considered in appendix C
1402 with sample grid spacings Δx and Δy that are equal to the footprint diameter, the noise is essentially
1403 uncorrelated at the grid spacing so that the lagged autocorrelations $\rho_h(2\Delta x)$ and $\rho_h(2\Delta y)$ in (D3)
1404 and (D4) are negligible. The noise variances (D3b) and (D4) for the geostrophically computed
1405 velocity components then reduce to

$$\sigma_{v_g}^2 = \frac{g^2}{f^2} \frac{1}{2\Delta x^2} \sigma_h^2 \quad (\text{D5})$$

$$\sigma_{u_g}^2 = \frac{g^2}{f^2} \frac{1}{2\Delta y^2} \sigma_h^2. \quad (\text{D6})$$

1407 For the fourth case of a footprint diameter of 0.5 km and an oversampled grid spacing of
1408 $0.25 \text{ km} \times 0.25 \text{ km}$ discussed in appendix C, the noise variances for u_g and v_g must use the
1409 full equations (D3b) and (D4). For this grid spacing that is half of the footprint diameter, the
1410 lagged autocorrelations $\rho_h(2\Delta x)$ and $\rho_h(2\Delta y)$ are 0.05, so the noise variances would be only
1411 slightly overestimated by (D5) and (D6).

1412 The noise standard deviations σ_{v_g} and σ_{u_g} computed from the square roots of the variance
1413 expressions (D5) and (D6) are listed in the fourth column of the top half of Table 1 in section 2.

1414 For the purposes of this calculation, we used the Coriolis parameter $f_{37N} = 8.77 \times 10^{-5} \text{ s}^{-1}$ at the

1415 central latitude 37°N of the domain of the model of the California Current System (CCS) that is
1416 used for Fig. E1 below and Figs. 2–5 in the text. The noise standard deviation for latitudes other
1417 than 37°N can be determined as explained in the table caption. For all four of the cases of footprint
1418 diameter and sampling grid considered in appendix C, the noise of the geostrophically computed
1419 velocity components is very large. Even for the coarsest footprint diameter of 2 km, the standard
1420 deviation of the noise in each velocity component is more than 0.5 m s^{-1} , which corresponds to a
1421 noise of about 0.7 m s^{-1} in speed. For most applications, the geostrophically computed velocity
1422 fields will have to be smoothed further to obtain scientifically useful instantaneous estimates of
1423 velocity. The effects of smoothing of the u_g and v_g noise are investigated in sections 3–5.

1424 The second-order derivatives of SSH in the form (D2b) of the definition of vorticity are approx-
1425 imated here by a succession of two 3-point centered differences¹. It can therefore be anticipated
1426 that SSH measurement noise will render estimates of geostrophically computed vorticity from
1427 the SWOT data products even noisier than the geostrophically computed velocity components
1428 considered above.

1429 The errors of vorticity ζ_g computed from 3-point centered differences of geostrophically com-
1430 puted velocity components u_g and v_g at neighboring grid points are given by Eq. (G.7) of C19. The
1431 variance of these vorticity errors is determined from the variances and covariances of the five terms
1432 in that equation. The variance $\sigma_{\zeta_g}^2$ as expressed by Eq. (G.8) in appendix G.1 of C19 is specific
1433 to the case of SSH observations on the same grid on which the SSH noise is uncorrelated, which
1434 was the case of interest in that study. The equation for an arbitrarily specified grid spacing and
1435 footprint diameter was not included in appendix G.1 of C19. The general expression is the same as
1436 Eq. (G.21) in appendix G.3 of C19 that is derived for the residual noise in smoothed estimates of
1437 vorticity, except that the smoothed variances on the left and right sides of that equation are replaced
1438 with unsmoothed variances, and the lagged autocorrelations of smoothed SSH are replaced with
1439 lagged autocorrelations of unsmoothed SSH. For a uniform grid spacing $\Delta y = \Delta x$, the resulting

¹The vorticity is estimated here from 3-point centered differences of geostrophically computed velocity components at adjacent grid points, which are themselves estimated as 3-point centered differences of SSH at adjacent grid points. This is equivalent to approximating the second derivatives of SSH in (D2b) from stencils that span five adjacent grid points. The velocity components could alternatively be estimated as 2-point centered differences at locations half way between adjacent grid points and the vorticity could then be estimated from 2-point centered differences of these velocity estimates. This is equivalent to approximating the second derivatives of SSH from stencils that span only three adjacent grid points. The noise variance of vorticity estimates is a factor-of-4 larger on the 3-point spans than on the 5-point spans used in this study.

1440 equation is

$$\sigma_{\zeta_g}^2 = \frac{g^2}{f^2} \frac{1}{(4\Delta x^2)^2} \left[20 + 4\rho_h(4\Delta x) - 32\rho_h(2\Delta x) + 8\rho_h(2\sqrt{2}\Delta x) \right] \sigma_h^2, \quad (\text{D7})$$

1441 where $\rho_h(2\Delta x)$, $\rho_h(2\sqrt{2}\Delta x)$ and $\rho_h(4\Delta x)$ are the autocorrelations of the SSH measurement noise
 1442 at spatial lags of $2\Delta x$, $2\sqrt{2}\Delta x$ and $4\Delta x$.

1443 For the cases of the three footprint diameters of 0.5 km, 1 km and 2 km considered in appendix
 1444 C, and with sample grid spacings Δx and Δy that are equal to the footprint diameter, the autocor-
 1445 relations at nonzero lags are negligible. The noise variance (D7) of the geostrophically computed
 1446 vorticity then reduces to Eq. (G.8) of C19, which is

$$\sigma_{\zeta_g}^2 = \frac{g^2}{f^2} \frac{20\sigma_h^2}{(4\Delta x^2)^2} \quad (\text{D8a})$$

$$= \frac{g^2}{f^2} \frac{5}{4\Delta x^4} \sigma_h^2. \quad (\text{D8b})$$

1447 For the fourth case of a footprint diameter of 0.5 km and an oversampled grid spacing of
 1448 $0.25 \text{ km} \times 0.25 \text{ km}$ considered in appendix C, the noise variance for ζ_g must use the full equation
 1449 (D7). For this grid spacing that is half of the footprint diameter, the lagged autocorrelations
 1450 $\rho_h(2\sqrt{2}\Delta x)$ and $\rho_h(4\Delta x)$ are both negligible and $\rho_h(2\Delta x) = 0.05$ as in (D3) and (D4).

1451 The amplification of the effects of SSH measurement noise from the sequential 3-point centered
 1452 differences used here to compute the vorticity geostrophically from SSH can be quantified by
 1453 noting that the multiplicative factor $(g/f)^2/(4\Delta x^2)^2$ in (D7) and in the non-reduced form (D8a)
 1454 arises from a combination of the factor g/f in the geostrophic relations (D1) and the product of
 1455 two factors $2\Delta x$ in the denominators of the 3-point centered differences approximations of the
 1456 derivatives in (D1) and (D2a). These factors transform the units of squared SSH to units of squared
 1457 vorticity. The remaining factor of $20\sigma_h^2$ in the numerators of (D7) and (D8a) shows that the centered
 1458 differencing and the existence of two terms in the vorticity equation (D2b) increase the SSH noise
 1459 variance by a factor of 20. This large amplification compared with the factor-of-2 amplification of
 1460 the effects of SSH noise variance in the geostrophically computed velocity components deduced
 1461 above from (D3a) is because the vorticity at a given grid point is computed from SSH observations
 1462 in a cross pattern of five grid points [see Eqs. (G.7b) and (G.7c) of C19]. On the grids for which

1463 (D8) is applicable, the SSH measurement errors at the five individual grid points are essentially
1464 uncorrelated with each other. The SSH measurement error at the central grid point appears four
1465 times in the expression for the geostrophically computed vorticity errors, so its contribution to the
1466 vorticity noise variance is 16 times the SSH noise variance σ_h^2 . Each of the other four grid points
1467 contributes σ_h^2 , thus resulting in a total vorticity noise variance of $20\sigma_h^2$.

1468 The noise standard deviations σ_{ζ_g} computed from the square roots of the variance expressions
1469 (D7) and (D8) are listed in the fifth column of the top half of Table 1 in section 2, again for
1470 the Coriolis parameter f_{37N} at latitude 37°N . The last column of Table 1 lists the vorticity noise
1471 standard deviations normalized by the Coriolis parameter f_{37N} , which is easier to interpret than
1472 the noise standard deviation in the units of ζ_g . The noise of ζ_g and ζ_g/f for latitudes other than
1473 37°N can be determined as explained in the table caption.

1474 For all four of the cases of footprint diameter and sampling grid considered in appendix C, the
1475 noise of the geostrophically computed vorticity is far too large for the vorticity estimates from any
1476 of the SWOT data products to be useful directly. Even for the coarsest footprint diameter of 2 km,
1477 the standard deviation of the ζ_g noise is nearly five times larger than the planetary vorticity f_{37N} at
1478 37°N . Additional smoothing of SWOT data will thus be even more imperative for geostrophically
1479 computed vorticity than for the geostrophically computed velocity. The effects of smoothing of ζ_g
1480 noise are investigated in sections 3–5.

1481 APPENDIX E

1482 **The spectral characteristics of the noise in SWOT estimates of velocity and vorticity**

1483 The swath-averaged along-track wavenumber spectral distributions of the noise variances $\sigma_{u_g}^2$,
1484 $\sigma_{v_g}^2$ and $\sigma_{\zeta_g}^2$ listed in the top half of Table 1 are derived in appendix I.1 of C19. While the variances
1485 σ_h^2 of the noise in unsmoothed SWOT estimates of SSH with the three footprint diameters of 0.5
1486 km, 1 km and 2 km considered in appendix C are assumed to be uniformly distributed with respect
1487 to wavenumber (white) as shown by the green, blue and purple dashed lines in Fig. A1, it is
1488 shown in this appendix that the corresponding wavenumber spectra of the noise in the unsmoothed
1489 geostrophically computed SWOT estimates of the across-track velocity component and the vorticity
1490 differ significantly from white.

1491 For the analysis that follows, we define the x and y dimensions to be across-track and along-track,
 1492 respectively. Consider first the wavenumber spectrum of the geostrophically computed across-track
 1493 velocity component u_g for an along-track sample grid spacing of Δy . The along-track spectrum of
 1494 the noise in SWOT estimates of u_g can be deduced from Eqs. (I.2a) and (I.5) in appendix I.1 of
 1495 C19, which give

$$S_{u_g}(l) = \frac{g^2}{f^2} 4\Delta x \Delta y k_N \sigma_h^2 |W_{3pt}(l, \Delta y)|^2 \quad (\text{E1a})$$

$$= \frac{g^2}{f^2} 2\Delta y |W_{3pt}(l, \Delta y)|^2 \sigma_h^2, \quad (\text{E1b})$$

1496 where

$$W_{3pt}(l, \Delta y) = \frac{\sin(2\pi l \Delta y)}{\Delta y} = \frac{\sin(\pi l / l_N)}{\Delta y} \quad (\text{E2})$$

1497 is the response function for along-track 3-point centered differences (see appendix H of C19) and
 1498 the variables $k_N = (2\Delta x)^{-1}$ and $l_N = (2\Delta y)^{-1}$ in (E1a) and (E2), respectively, are the Nyquist
 1499 wavenumbers in the across-track and along-track dimensions. Eqs. (E1) and (E2) are valid for any
 1500 specified grid spacings Δx and Δy . Because of the presence of $W_{3pt}(l, \Delta y)$ on the right sides of
 1501 (E1a) and (E1b), the wavenumber spectrum of u_g noise deviates dramatically from white (see Fig.
 1502 E1 below).

1503 The along-track wavenumber spectrum of noise in the geostrophically computed along-track
 1504 velocity component v_g for an across-track sample grid spacing of Δx is given by Eq. (I.8a) in
 1505 appendix I.1 of C19, which is

$$S_{v_g}(l) = \frac{g^2}{f^2} 4\Delta x \Delta y \sigma_h^2 \int_0^{k_N} |W_{3pt}(k, \Delta x)|^2 dk, \quad (\text{E3a})$$

1506 where $W_{3pt}(k, \Delta x)$ is the response function for across-track 3-point centered differences analogous
 1507 to (E2), but with across-track wavenumber k and grid spacing Δx rather than along-track wavenum-
 1508 ber l and grid spacing Δy . The integral on the right side of (E3a) is shown by Eq. (I.9) in appendix
 1509 I.1 of C19 to be $(4\Delta x^3)^{-1}$. This reduces (E3a) to Eq. (I.10a) of C19, which is

$$S_{v_g}(l) = \frac{g^2}{f^2} \frac{\Delta y}{\Delta x^2} \sigma_h^2. \quad (\text{E3b})$$

1510 In contrast to the wavenumber spectrum (E1) of noise in SWOT estimates of u_g , the wavenumber
 1511 spectrum (E3) of noise in SWOT estimates of v_g is independent of wavenumber l and is therefore
 1512 white. This is because the derivative in the geostrophic relation (D1b) is orthogonal to the along-
 1513 track dimension of the spectrum.

1514 The along-track wavenumber spectrum of the noise in SWOT estimates of vorticity computed
 1515 from 3-point centered differences of u_g and v_g is given by Eq. (I.24a) of C19, which is

$$S_{\zeta_g}(l) = \frac{g^2}{f^2} 2\Delta y \left(\frac{3}{8\Delta x^4} + \frac{1}{\Delta x^2} |W_{3pt}(l, \Delta y)|^2 + |W_{3pt}(l, \Delta y)|^4 \right) \sigma_h^2. \quad (\text{E4})$$

1516 The greater complexity of this equation for the spectrum $S_{\zeta_g}(l)$ of vorticity noise compared with
 1517 equations (E1b) and (E3) for the spectra $S_{u_g}(l)$ and $S_{v_g}(l)$ of noise in the geostrophically computed
 1518 velocity components arises from the double differentiation of SSH in (D2b) that is required to
 1519 compute the noise in ζ_g from the SSH noise, and the fact that vorticity consists of a sum of two
 1520 terms. The wavenumber spectrum of ζ_g noise deviates from white because of the presence of
 1521 $W_{3pt}(l, \Delta y)$ in the two terms on the right side of (E4).

1522 A key point to note from (E1), (E3) and (E4) is that the wavenumber spectra of the noise in the
 1523 derivative variables u_g , v_g and ζ_g have all been expressed in terms of the SSH noise variance σ_h^2
 1524 that is the fundamental characterization of the uncorrelated SWOT measurement errors. The noise
 1525 spectra for the derivative variables could alternatively be expressed in terms of the white (constant)
 1526 along-track wavenumber spectrum $S_h(l)$ of the SSH measurement noise by inverting (C3) that
 1527 relates σ_h^2 to the integral of the constant white noise spectrum $S_h(l)$ by

$$\sigma_h^2 = l_N S_h(l) = \frac{S_h(l)}{2\Delta y}. \quad (\text{E5})$$

1528 In the forms (E1b), (E3b) and (E4), the equations for the noise in SWOT estimates of u_g , v_g and
 1529 ζ_g are all valid for any specified σ_h^2 and sample grid spacings Δx and Δy . The spectra for the three
 1530 footprint diameters of 0.5 km, 1 km and 2 km considered in appendix C can thus be determined by
 1531 replacing σ_h^2 in (E1), (E3) and (E4) with the pre-launch estimates of $\sigma_{0.5\text{km}}^2$, $\sigma_{1\text{km}}^2$ and $\sigma_{2\text{km}}^2$ that are
 1532 given by (C5), (C3) and (C8), respectively. Moreover, these pre-launch estimates can be replaced
 1533 with the actual values determined after launch from in-orbit data or with smaller values that may
 1534 be obtained in the future from improvements in the processing of SWOT data.

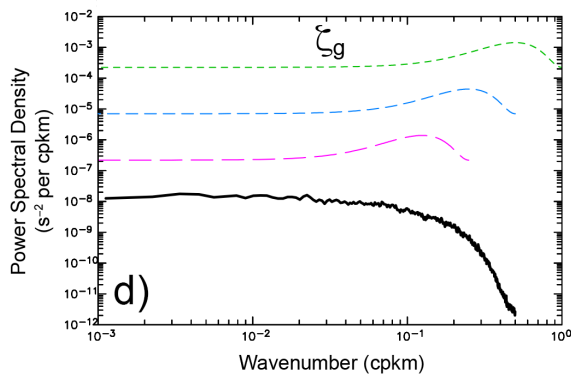
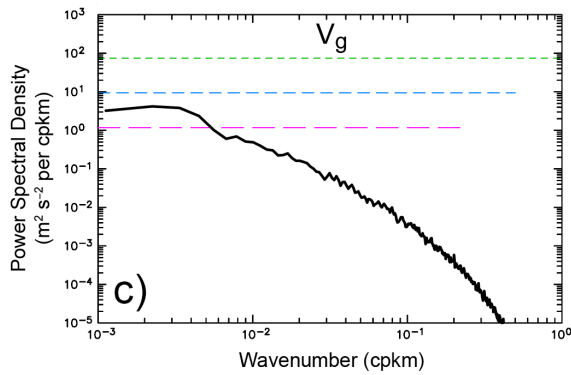
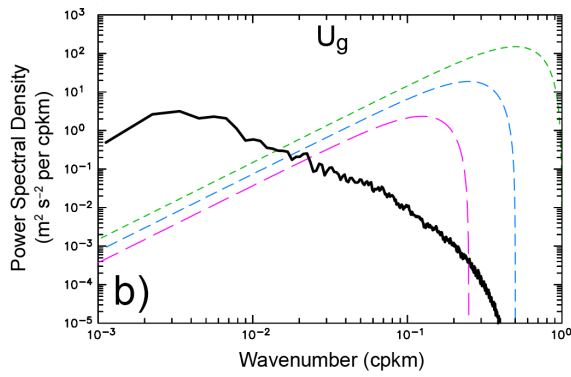
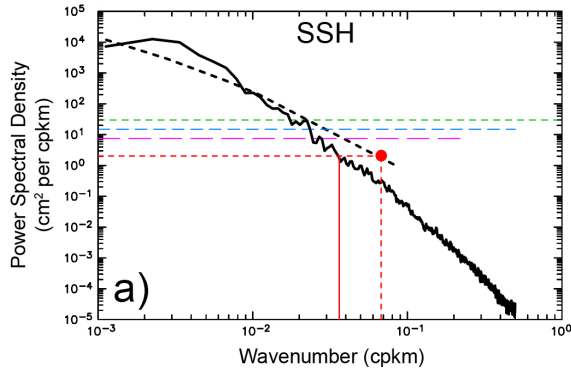
1535 The along-track wavenumber spectra of noise in u_g , v_g and ζ_g obtained from (E1b), (E3b) and
1536 (E4) for the footprint diameters of 0.5 km, 1 km and 2 km are shown, respectively, by the green,
1537 blue and purple dashed lines in Fig. E1 for the cases of uniform sample grid spacings of $\Delta x = \Delta y$
1538 equal to each of the three footprint diameters. The SSH noise spectra and the 68th percentile of the
1539 globally distributed SSH spectra in Fig. E1a are the same as in Fig. A1, but with a larger dynamic
1540 range of the ordinate to accommodate the solid black line that is the alongshore wavenumber
1541 spectrum of error-free SSH computed from a snapshot of the CCS model used in section 5. Note
1542 that alongshore for this CCS model corresponds closely to along-track for descending overpasses
1543 with the inclination of the SWOT orbit (see Fig. 3). The black lines in Figs. E1b, c and d are
1544 the alongshore wavenumber spectra of error-free u_g , v_g and ζ_g computed from the same snapshot
1545 of the CCS model. These signal spectra are included to provide a sense of how the along-track
1546 wavenumber distributions of noise variance compare with the wavenumber distributions of the
1547 signal variance in the CCS region, which may be representative of many regions of the world
1548 ocean.

1563 Before discussing the spectra in Fig. E1, we note a minor caveat to the analytical expressions
1564 (E1), (E3) and (E4). These equations require the use of a constant value for the Coriolis parameter
1565 f . For the spectra in Figs. E1b, c and d, we used the value of $f_{37N} = 8.77 \times 10^{-5} \text{ s}^{-1}$ for the
1566 central latitude of 37°N of the CCS model domain. Over the 32.5°N to 42°N latitude range of
1567 the model, the Coriolis parameter varies by $\pm 11\%$ from f_{37N} . Because f in this latitude range
1568 varies approximately linearly with latitude, and because the statistics of the measurement noise
1569 are assumed to be homogeneous for the calculations in this study, the latitudinal variation of f is
1570 a minor issue. It is shown in Figs. 13 and 14 of C19 that the theoretical noise spectra computed
1571 from (E1b), (E3b) and (E4) are essentially identical to the noise spectra computed empirically from
1572 simulated SWOT measurement noise in the CCS model.

1573 Consider first the SSH signal and noise spectra in Fig. E1a. To the extent that the CCS
1574 model considered here is an accurate representation of reality, this figure raises a concern about
1575 whether the goal of resolving SSH variability down to a wavelength of 15 km will be achieved by
1576 SWOT. The SWOT documentation adopts a signal-to-noise ratio of 1 as the metric for defining
1577 the resolution of SWOT estimates of SSH². As discussed in appendix A, this goal is based on the

²For reasons that are discussed in section 5 of C19, a signal-to-noise ratio of 1 is too small for characterization of resolution capability. C19 advocate a signal-to-noise variance ratio of at least 4 and preferably 10 (standard deviation ratios of 2 and 3.16). For the purposes of the present discussion, however, we will discuss resolution in the context of the signal-to-noise ratio of 1 adopted by the SWOT Project.

Wavenumber Spectra for 0.5, 1 and 2 km Footprints



1549 FIG. E1. Swath-averaged wavenumber power spectral densities of signals (solid black lines) and noise in SWOT
1550 estimates of a) SSH; b) u_g ; c) v_g ; and d) ζ_g . The signal spectra were computed in the alongshore dimension from
1551 the ROMS model of the California Current System (CCS) considered here for which descending swaths of SWOT
1552 are approximately parallel to the coast (see Fig. 3). The black dashed line in a) is the 68th spectrum of SSH
1553 from Fig. A1 and the horizontal red dashed line is the science requirement specification (A2) for uncorrelated
1554 measurement noise after smoothing with the half-power filter cutoff wavelength of 15 km shown by the vertical
1555 red dashed line that intersects the horizontal red dashed line at the red dot. The intersection of the SSH spectrum
1556 from the CCS model with the horizontal red dashed line occurs at a wavelength of about 28 km, indicated by
1557 the vertical solid red line. The green, blue and purple dashed lines are, respectively, the noise spectra for each
1558 variable for footprint diameters of 0.5 km on a 0.5 km \times 0.5 km grid, 1 km on a 1 km \times 1 km grid, and 2 km
1559 on a 2 km \times 2 km grid with the corresponding SSH measurement error standard deviations of $\sigma_{0.5\text{km}} = 5.48$ cm,
1560 $\sigma_{1\text{km}} = 2.74$ cm and $\sigma_{2\text{km}} = 1.37$ cm derived in appendix C. The noise spectra for geostrophically computed
1561 velocity components and vorticity are based on a Coriolis parameter of $f_{37\text{N}} = 8.75 \times 10^{-5} \text{ s}^{-1}$ at the central
1562 latitude 37°N of the CCS model.

1578 science requirement (A2) that the along-track wavenumber spectrum of 15-km smoothed SWOT
1579 measurement noise intersects the 68th percentile of the extrapolated globally distributed SSH signal
1580 spectra at a wavelength of 15 km (see Fig A1). This intersection is indicated by the red dot in
1581 Fig. E1a. The along-track wavenumber spectrum of SSH from the CCS model has a steeper
1582 rolloff than the 68th percentile spectrum of SSH. As a consequence, the wavenumber spectrum
1583 of smoothed SWOT measurement noise intersects the SSH spectrum from the CCS model at the
1584 lower wavenumber of about $l = 0.035$ cpkm shown by the vertical solid red line. This corresponds
1585 to a wavelength of about 28 km.

1586 Some of the discrepancy between the 28 km resolution inferred from the CCS model and the
1587 15 km resolution inferred from the 68th percentile spectrum may be attributable to inadequacies
1588 in the CCS model. As summarized in section 2 of C19, this model does not include tides and
1589 was forced by seasonal cycle winds. The model also has a high dissipation that attenuates internal
1590 wave variability. Moreover, the vertical and horizontal grid resolutions are not adequate to resolve
1591 the full spectrum of internal waves. It can thus be expected that the model underestimates the
1592 variability on scales smaller than about 50 km. However, from the discussion in appendix F of C19
1593 of the wavenumber spectra from this CCS model and from two versions of a model of the Gulf

1594 Stream region (see Figs. F.3 and F.4 of C19), it appears that the inadequacies of the CCS model
1595 are not sufficient to explain all of the difference between the 28 km resolution inferred from the
1596 CCS model and the 15 km resolution inferred from the 68th percentile of the globally distributed
1597 SSH spectra.

1598 On the other hand, the 68th percentile spectrum of SSH is based on nadir altimeter data that resolve
1599 SSH only down to wavelengths of about 70 km (Xu and Fu 2012). Little is known observationally
1600 about SSH variability on scales shorter than 70 km. The spectra computed from the nadir altimeter
1601 data from which the 68th percentile spectrum was derived were extrapolated from 70 km down
1602 to the wavelength of 15 km. Some, and perhaps even much, of the discrepancy between the
1603 28 km resolution inferred from the CCS model and the 15 km resolution inferred from the 68th
1604 percentile spectrum may therefore be attributable to inaccuracies of this extrapolation. Concerns
1605 about the validity of the 68th percentile SSH spectrum at wavelengths shorter than 100 km have
1606 been discussed in much greater detail by Callies and Wu (2019). An important contribution of the
1607 SWOT mission will be to obtain the first observations of SSH variability at these smaller scales
1608 that have not previously been observable from space or in situ data.

1609 The wavenumber spectra of u_g and v_g signal and noise shown in Figs. E1b and c differ rather
1610 dramatically from each other. The structure of the wavenumber spectrum of u_g noise is imposed by
1611 the fact that the filtering from the 3-point centered difference estimate of the derivative in (D1a) is
1612 in the same along-track dimension y as the wavenumber spectrum. The u_g noise spectra therefore
1613 exhibit the $\sin^2(2\pi l\Delta y)$ structures of the squared response function $|W_{3pt}(l, \Delta y)|^2$ in (E2). (This
1614 \sin^2 structure is distorted by the logarithmic abscissa in Fig. E1b.) In contrast, the filtering from
1615 the 3-point centered difference estimate of the derivative in the expression (D1b) for v_g is in the
1616 across-track dimension x that is orthogonal to the along-track dimension of the spectrum. It can
1617 be seen from (E3a) that the effects of this across-track filtering are integrated in the 1-dimensional
1618 along-track wavenumber spectra of v_g noise, thus resulting in a constant multiplier on the right
1619 side of the equation. The resulting spectra of v_g noise as expressed by (E3b) are constant (i.e.,
1620 white) and proportional to the value of σ_h^2 that is appropriate for the footprint diameter of interest.
1621 If the 1-dimensional spectra presented here were in the across-track dimension rather than the
1622 along-track dimension, the structures of the spectra of u_g and v_g noise would be reversed. Because
1623 of the limited across-track extent of SWOT measurement swaths, across-track spectra cannot be

1624 computed directly from SWOT data with the high wavenumber resolution of the along-track spectra
1625 in Fig. E1.

1626 It can be seen from Fig. E1b that the spectral power of the across-track velocity component u_g
1627 exceeds the noise power for wavenumbers below about 0.02 cpkm (wavelengths longer than 50 km),
1628 but this signal variance would be masked in maps or along-track profiles of u_g by the very energetic
1629 noise at higher wavenumbers unless the u_g estimates are smoothed in post-processing to attenuate
1630 this small-scale variability. In the case of the along-track velocity component v_g (Fig. E1c), the
1631 spectral power of the v_g noise exceeds the signal power at all wavenumbers for footprint diameters
1632 of 0.5 km and 1 km. Without additional smoothing, the v_g signal in the CCS model would therefore
1633 be undetectable on any scales in SWOT data with these two footprint sizes. For a larger footprint
1634 diameter of 2 km, the v_g noise spectrum exceeds the signal power only at wavenumbers lower than
1635 about 0.005 cpkm (wavelengths longer than about 200 km).

1636 The signal and noise spectra for ζ_g are shown in Fig. E1d. The structures of the spectra of ζ_g
1637 noise consist of a blend of the structures of the spectra of u_g and v_g noise because the expression
1638 (D2) for the geostrophically computed vorticity involves derivatives in both the along-track and
1639 the across-track dimensions. The spectral power of the noise far exceeds the signal power for all
1640 three footprint diameters. Even for the coarsest footprint diameter of 2 km, the noise power is more
1641 than an order of magnitude higher than the signal power at all wavenumbers. Without additional
1642 smoothing in post-processing, the vorticity signal would therefore not be detectable on any scales,
1643 even when computed from the SWOT data with a footprint diameter of 2 km.

References

- 1644 Ballarotta M., C. Ubelmann, M.-I. Pujol, G. Taburet, F. Fournier, J.-F. Legeais, Y. Faugere, A.
1645 Delepoule, D. Chelton, G. Dibarboure, and N. Picot, 2019: On the resolutions of ocean altimetry
1646 maps. *Ocean Sci.*, **15**, 1091–1109.
- 1647 Callies, J., and W. Wu 2019: Some expectations for submesoscale sea surface height variance
1648 spectra. *J. Phys. Oceanogr.*, **49**, 2271–2289.
- 1649 Chelton, D. B., 2019: The Wavenumber Spectra and Standard Deviations of Uncorrelated Errors
1650 in SWOT Measurements of Sea-Surface Height for Various Footprint Sizes. White paper posted
1651 on JPL SWOT website <https://swot.jpl.nasa.gov/documents.htm> (9 pp.).

1652 Chelton, D. B., J. C. Ries, B. J. Haines, L.-L. Fu and P. S. Callahan, 2001: Satellite altimetry. In
1653 *Satellite Altimetry and the Earth Sciences: A Handbook of Techniques and Applications*, L.-L.
1654 Fu and A. Cazenave, Eds., Academic Press, pp. 1–131.

1655 Chelton, D. B., M. G. Schlax, and R. M. Samelson, 2011: Global observations of nonlinear
1656 mesoscale eddies. *Prog. Oceanogr.*, **91**, 167–216.

1657 Chelton, D. B., M. G. Schlax, R. M. Samelson, J. T. Farrar, M. J. Molemaker, J. C. McWilliams
1658 and J. Gula 2019: Prospects for future satellite estimation of small-scale variability of ocean
1659 surface velocity and vorticity. *Prog. Oceanogr.*, **173**, 256–350.

1660 Durand, M., L.-L. Fu, D. P. Lettenmaier, D. E. Alsdorf, E. Rodríguez and D. Esteban Fernandez,
1661 2010: The surface water and ocean topography mission: observing terrestrial surface water and
1662 oceanic submesoscale eddies. *Proc. IEEE*, **98**, 766–779.

1663 Fu, L.-L., and R. Ferrari, 2008: Observing oceanic submesoscale processes from space. *Eos*, **89**,
1664 488–489.

1665 Fu, L.-L., and E. Rodríguez, 2004: High-resolution measurement of ocean surface topography by
1666 radar interferometry for oceanographic and geophysical applications. In *The State of the Planet:
1667 Frontiers and Challenges in Geophysics, Geophys. Monogr. Ser.*, vol. 150, edited by R. S. J.
1668 Sparks and C. J. Hawkesworth, pp. 209–224, AGU, Washington, D.C.

1669 Fu, L.-L., and C. Ubelmann, 2014: On the transition from profile altimeter to swath altimeter for
1670 982 observing global ocean surface topography. *J. Atmos. Oceanic Technol.*, **31**, 560–568.

1671 JPL Internal Document, 2017a: SWOT Project Mission Performance and Error Budget. Jet
1672 Propulsion Laboratory Document D-79084 Revision A, April 7 2017, 83 pp.

1673 JPL Internal Document, 2017b: KaRIn: Ka-Band Radar Interferometer Onboard Processor (OBP)
1674 Algorithm Theoretical Basis Document (ATBD). Jet Propulsion Laboratory Document D-79130,
1675 Revision A, November 3 2017, 73 pp.

1676 JPL Internal Document, 2017c: SWOT Simulator Documentation. Jet Propulsion Laboratory,
1677 Release 2.3.0, March 15 2017, 44 pp.

1678 JPL Internal Document, 2018: Surface Water and Ocean Topography Mission (SWOT) Project Sci-
1679 ence Requirements Document. Jet Propulsion Laboratory Document D-61923, Rev B, January
1680 24 2018, 29 pp.

1681 JPL Internal Document, 2020: Surface Water and Ocean Topography (SWOT) Project SWOT
1682 Product Description. Jet Propulsion Laboratory Document D-56407, Revision A (DRAFT),
1683 August 6 2020, 78 pp.

1684 Molemaker, M. J., J. C. McWilliams and W. K. Dewar, 2015: Submesoscale instability and
1685 generation of mesoscale anticyclones near a separation of the California undercurrent. *J. Phys.*
1686 *Oceanogr.*, **45**, 613–629.

1687 Pascual, A., Y. Faugere, G. Larnicol, P.-Y. Le Traon, 2006: Improved description of the ocean
1688 mesoscale variability by combining four satellite altimeters. *Geophys. Res. Lett.*, **33**.
1689 doi:10.1029/2005GL024633.

1690 Qiu, B., T. Nakano, S. Chen, and P. Klein, 2017: Submesoscale transition from geostrophic
1691 flows to internal waves in the northwestern Pacific upper ocean. *Nature Comm.*, **8**, 14055,
1692 doi:10.1038/ncomms14055.

1693 Qiu, B., S. Chen, P. Klein, J. Wang, H. Torres, L.-L. Fu and D. Menemenlis, 2018: Seasonality
1694 in transition scale from balanced to unbalanced motions in the world ocean. *J. Phys. Oceanogr.*,
1695 **48**, 591–605.

1696 Rocha, C. B., T. K. Chereskin, S. T. Gille and D. Menemenlis, 2016: Mesoscale to submesoscale
1697 wavenumber spectra in Drake Passage. *J. Phys. Oceanogr.*, **46**, 601–620.

1698 Schlax, M. G., and D. B. Chelton, 2003: The accuracies of crossover and parallel-track estimates
1699 of geostrophic velocities from TOPEX/POSEIDON and Jason altimeter data. *J. Atmos. Oceanic*
1700 *Technol.*, **20**, 1196–1211.

1701 Ubelmann, C., P. Klein, L.-L. Fu, 2015: Dynamic interpolation of sea surface height and potential
1702 applications for future high-resolution altimetry mapping. *J. Atmos. Oceanic Technol.*, **32**,
1703 177–184.

1704 Xu, Y., and L.-L. Fu 2012: The Effects of altimeter instrument noise on the estimation of the
1705 wavenumber spectrum of sea surface height. *J. Phys. Oceanogr.*, **42**, 2229–2233.

1706 Yu, X., A. L. Ponte, N. Lahaye, Z. Caspar-Cohen and D. Menemenlis, 2021: Geostrophy assessment
1707 and momentum balance of the global oceans in a tide- and eddy-resolving model. *J. Geophys.*
1708 *Res.*, **126**, e2021JC017422.